

# New constraints on Lorentz invariance violation from combined linear and circular optical polarimetry of extragalactic sources

Roman Gerasimov<sup>1</sup>, Praneet Bhoj<sup>1</sup> and Fabian Kislak<sup>2</sup>

<sup>1</sup> Center for Astrophysics and Space Sciences, University of California, San Diego, La Jolla, California 92093, USA

<sup>2</sup> Department of Physics & Astronomy and Space Science Center, University of New Hampshire, Durham, NH 03824, USA

\* Correspondence: romang@ucsd.edu (R. Gerasimov), fabian.kislak@unh.edu (F. Kislak)

**Abstract:** Expanding on our prior efforts to search for Lorentz invariance violation (LIV) using linear optical polarimetry of extragalactic objects [1–3], we propose a new method that combines linear and circular polarization measurements. While existing work focused on the tendency of LIV to reduce the linear polarization degree, this new method additionally takes into account the coupling between photon helicities induced by some models. This coupling can generate circular polarization as light propagates, even if there is no circular polarization at the source. Combining significant detections of linear polarization of light from extragalactic objects with the absence of a detection of circular polarization in most measurements results in significantly tighter constraints on LIV. The analysis is carried out in the framework of the Standard-Model Extension (SME), an effective field theory framework to describe low-energy effects of an underlying more fundamental quantum gravity theory. We evaluate the performance of our method by deriving constraints on mass dimension  $d = 4$  CPT-even SME coefficients from a small set of archival circular and linear optical polarimetry and compare them to similar constraints derived in previous work with far larger sample sizes and based on linear polarimetry only. The new method yields constraints that are an order of magnitude tighter even for our modest sample size of 21 objects. Based on the demonstrated gain in constraining power from scarce circular data, we advocate for the need in future extragalactic circular polarization surveys.

**Keywords:** Lorentz invariance; Standard-Model extension; AGN; Polarization



**Citation:** Gerasimov, R.; Bhoj, P.; Kislak, F. New constraints on Lorentz invariance violation from combined linear and circular optical polarimetry of extragalactic sources. *Preprints* 2021, 1, 0. <https://doi.org/>

Received:  
Accepted:  
Published:

**Publisher's Note:** MDPI stays neutral with regard to jurisdictional claims in published maps and institutional affiliations.

## 1. Introduction

Einstein's theory of general relativity provides an excellent classical model of gravitation, and the Standard Model of particle physics is a well-established quantum theoretical model of particles and all forces except gravity. Together, they provide a well-tested description of nature at experimentally attainable energies. However, at the Planck scale ( $E_P \approx 1.22 \times 10^{19}$  GeV), a quantum-consistent theory of gravity is required. A lack of direct experimental input to guide the development of the theory poses a significant challenge. Additionally, the failure of the Large Hadron Collider to detect evidence of physics beyond the Standard Model, including supersymmetry, presents a challenge to many candidate theories [4]<sup>1</sup>.

Several theories that attempt to unify gravity and the Standard Model at the Planck scale suggest that there may be deviations from Lorentz invariance at this energy scale [6–13]. This motivates detailed tests of Lorentz symmetry despite the fact that such deviations are expected to be highly suppressed at energies  $E \ll E_P$  [14,15]. Tests of this kind are routinely carried out by high-energy physics experiments [16–20], but reaching progressively higher energies will eventually become unfeasible. Astrophysical tests in the photon sector have proven to be

<sup>1</sup> Indications of beyond-the-standard-model physics at the  $3.1\sigma$  level in B quark decays were presented by the LHCb collaboration after completion of this work [5].

particularly powerful because tiny deviations from the speed of light as a result of Lorentz invariance violations (LIV) accumulate when photons propagate over very large distances, resulting in potentially observable effects.

If Lorentz symmetry is broken, the phase velocity of light in vacuum may depend on photon energy, polarization, and direction of propagation. The Standard-Model Extension (SME) is an effective field theory framework, which extends the Standard Model of particle physics by introducing new, Lorentz and CPT violating terms in the Lagrangian, while conserving charge, energy, and momentum [15,21–24]. Within this framework, group theory considerations allow a classification of potential quantum gravity models in three broad classes with respect to their Lorentz violating effects: birefringent and non-birefringent CPT-even, as well as CPT-odd models, all of which result in a birefringent photon dispersion [15]. Non-birefringent models result in a dispersion relation that may depend on photon energy and propagation direction, but will not exhibit any helicity dependence. The strongest constraints on models of this kind result from astrophysical time-of-flight measurements of gamma-rays emitted by transient events or variable sources [25–34].

Birefringent CPT-even and CPT-odd models can be constrained much more strongly by polarization measurements because the measurement is essentially that of a phase difference between the two polarization modes rather than photon arrival times [2,15]. Most astrophysical radiation processes result in very low circular polarization, but linear polarization can be significant. Birefringence then results in a rotation of the linear polarization direction as photons propagate. If the strength of this effect depends on energy, an energy dependence of the polarization direction will be observed, even if the polarization at the source does not depend on energy. When measuring photon polarization over a broad bandwidth, this rotation results in an effective reduction of the observable polarization fraction. Hence, any observation of linear polarization of light from a distant object can be used to constrain the magnitude of birefringence due to LIV [15]. Some of the strongest constraints of birefringent LIV models come from X-ray polarization measurements [35–39]. However, observations of a single source cannot be used to constrain anisotropic models. In CPT-even models the LIV terms result in a coupling between the two helicity states, which means neither linear nor circular polarization of light are preserved during propagation. The helicity of  $\pm 2$  of the coupling necessarily results in anisotropy.

Within the SME, models can be classified based on their low-energy behavior described above, as well as an expansion in terms of the mass dimension  $d$  of corresponding operators, and an expansion in spherical harmonics describing anisotropic effects. The terms of the expansion are then characterized by a set of coefficients which can be constrained by experiment [40]. In the photon sector, terms of odd mass dimension  $d$  represent CPT-odd models and even- $d$  terms represent CPT-even models. Odd- $d$  models are characterized by a set of complex coefficients with  $(d - 1)^2$  real components. Non-birefringent, even- $d$  models are characterized by  $(d - 1)^2$  real components, and birefringent even- $d$  models have  $2(d - 1)^2 - 8$  coefficients with the same number of real components [15].

We have developed a method to combine polarization measurements from many objects in order to individually constrain coefficients of a given mass dimension. By applying this method to a large number of optical polarization measurements, we have obtained the strongest constraints on individual coefficients to date [1–3,40]. In essence, we sample the SME coefficient space and for each set of coefficients calculate the likelihood to make all given polarization measurements with the published uncertainties on the linear polarization values. Here, we improve on our approach for CPT-even models characterized by even- $d$  coefficients by incorporating circular polarization measurements of active galactic nuclei in the optical band. As we will show in Section 3, in these models the coupling between left-handed and right-handed circular polarization will dominate the reduction of observable

linear polarization in most cases. Hence, circular polarization measurements provide an important additional constraint resulting in significantly tighter constraints than with linear polarization alone. In this paper, we extend our method to include circular polarization data. We then apply the method to a set of 21 linear and circular polarization measurements of quasars in order to derive new constraints on the 10 birefringent SME coefficients of mass dimension  $d = 4$ . Our new constraints are an order of magnitude stronger than existing constraints on the individual  $d = 4$  photon-sector SME coefficients.

The remainder of the paper is structured as follows. In Section 2 we briefly describe the photon-sector Lagrangian and photon dispersion relation in the minimal SME, and then derive the underlying equations of our method in Section 3. Section 4 summarizes the assumptions about linear and circular polarization at the source that we make in our analysis. The data set is described in Section 5. We explain the Markov-Chain Monte Carlo method used to sample the SME coefficient space, and give the results of our analysis in Section 6, and conclude with a summary in Section 7.

## 2. Photon sector SME

For photons in vacuum, SME operates by adding two extra terms to the standard Lagrangian of the electromagnetic field, such that the total Lagrangian reads [15,41]:

$$\mathcal{L} = -\frac{1}{4}F_{\alpha\beta}F^{\alpha\beta} + \left[ \frac{1}{2}\varepsilon^{\gamma\delta\alpha\beta}A_\delta(\hat{k}_{AF})_\gamma F_{\alpha\beta} - \frac{1}{4}F_{\gamma\delta}(\hat{k}_F)^{\gamma\delta\alpha\beta}F_{\alpha\beta} \right] \quad (1)$$

where the added terms are placed in brackets,  $F_{\alpha\beta}$  is the field tensor,  $A_\alpha$  is the 4-potential of the field ( $F_{\alpha\beta} = \delta_\alpha A_\beta - \delta_\beta A_\alpha$ ),  $\varepsilon^{\gamma\delta\alpha\beta}$  is the Levi-Civita symbol,  $(\hat{k}_{AF})_\gamma$  and  $(\hat{k}_F)^{\gamma\delta\alpha\beta}$  are the Lorentz invariance-violating operators,

$$(\hat{k}_{AF})_\gamma = \sum_{d \geq 3, d \in \text{odd}} \left( k_{AF}^{(d)} \right)_\gamma^{\lambda_1 \dots \lambda_{(d-3)}} \delta_{\lambda_1 \dots \lambda_{(d-3)}} \quad (2)$$

$$(\hat{k}_F)^{\gamma\delta\alpha\beta} = \sum_{d \geq 4, d \in \text{even}} \left( k_F^{(d)} \right)^{\gamma\delta\alpha\beta\lambda_1 \dots \lambda_{(d-4)}} \delta_{\lambda_1 \dots \lambda_{(d-4)}} \quad (3)$$

and the sets of coefficients  $\left( k_{AF}^{(d)} \right)_\gamma^{\lambda_1 \dots \lambda_{(d-3)}}$  and  $\left( k_F^{(d)} \right)^{\gamma\delta\alpha\beta\lambda_1 \dots \lambda_{(d-4)}}$  quantify the effect of the SME. The coefficients are grouped by the mass dimension of the corresponding term in the Lagrangian,  $d$ . All coefficients must vanish identically if the standard electromagnetic Lagrangian holds perfectly and no LIV effects are present in the universe.

The added terms allow for all possible violations of Lorentz invariance in rotations and boosts of the electromagnetic field, while maintaining Lorentz invariance for the inertial frame of the observer and thereby ensuring that physics is independent of the chosen system of coordinates [23]. Specifically, non-zero components of  $\left( k_F^{(d)} \right)^{\gamma\delta\alpha\beta\lambda_1 \dots \lambda_{(d-4)}}$  give rise to CPT-even terms in the Lagrangian that preserve the CPT symmetry, while non-zero components of  $\left( k_{AF}^{(d)} \right)_\gamma^{\lambda_1 \dots \lambda_{(d-3)}}$  result in CPT-odd terms that violate both CPT and Lorentz invariance.

In this work, we follow [23] and further restrict our attention to the so-called *minimal SME* that only contains terms of renormalizable mass dimensions, i.e.  $d \leq 4$ . This simplification is motivated by the scarcity of available circular optical polarimetry of extragalactic sources, which necessitates a theory with the smallest number of free parameters in order to derive reliable constraints. We however emphasize that the method presented here is universal and can be easily extended to higher mass dimensions ( $d > 4$ ) if provided with sufficient amount of experimental data from future polarimetric surveys and necessary computational resources.

Under minimal SME, only the  $d = 3$  term in Equation (2) and  $d = 4$  term in Equation (3) remain, resulting in the following Lagrangian:

$$\mathcal{L} = -\frac{1}{4}F_{\alpha\beta}F^{\alpha\beta} + \left[ \frac{1}{2}\varepsilon^{\gamma\delta\alpha\beta}A_\delta \left( k_{AF}^{(3)} \right)_\gamma F_{\alpha\beta} - \frac{1}{4}F_{\gamma\delta} \left( k_F^{(4)} \right)^{\gamma\delta\alpha\beta} F_{\alpha\beta} \right] \quad (4)$$

where  $k_{AF}^{(3)}$  has the units of mass and 4 independent components and  $k_F^{(4)}$  is dimensionless and has  $4^4 = 256$  components, of which only 19 are independent due to the required symmetries:  $(k_F^{(4)})_{\alpha\beta\gamma\delta} + (k_F^{(4)})_{\alpha\gamma\delta\beta} + (k_F^{(4)})_{\alpha\delta\beta\gamma} = 0$ ,  $(k_F^{(4)})^{\alpha\beta}{}_{\alpha\beta} = 0$  and  $(k_F^{(4)})_{\alpha\beta\gamma\delta} = -(k_F^{(4)})_{\alpha\beta\delta\gamma} = -(k_F^{(4)})_{\beta\alpha\gamma\delta} = (k_F^{(4)})_{\gamma\delta\alpha\beta}$  [23].

The equations of motion associated with the Lagrangian in Equation (4) are the modified Maxwell equations with SME-induced LIV. Two leading order plain wave solutions (eigenmodes) exist with orthogonal polarization states and a phase shift. Following the conventions in [15,41] we write out the modified dispersion relations for the two solutions as follows:

$$E = \left( 1 - \zeta^0 \pm \sqrt{(\zeta^1)^2 + (\zeta^2)^2 + (\zeta^3)^2} \right) \mathbb{P} \quad (5)$$

where  $E$  and  $\mathbb{P}$  are the energy and momentum of the photon (setting  $c = \hbar = 1$ ) and  $\zeta^\alpha$  are functions of the direction of arrival at the observer and the wavelength of the photon with the functional forms determined by the components of  $k_F^{(4)}$  and  $k_{AF}^{(3)}$ . Specifically,  $\zeta^\alpha$  are defined such that  $\zeta^0$  depends on 9 components of  $k_F^{(4)}$ ,  $\zeta^1$  and  $\zeta^2$  depend on the remaining 10 components of  $k_F^{(4)}$  and  $\zeta^3$  depends only on the components of  $k_{AF}^{(3)}$ . The orthogonality of the two eigenmodes in Equation (5) requires  $\langle + | - \rangle = 0$ , where  $|+\rangle$  and  $|-\rangle$  are the Jones vectors of the corresponding polarization states. The observed electromagnetic wave is a superposition of both eigenmodes.

A non-zero value of  $\zeta^0$  modifies the speed of propagation ( $E/p$ ) for both eigenmodes equally and independently of the photon wavelength for renormalizable mass dimensions. Since  $\zeta^0$  has no effect on polarization, no constraints on its value can be derived in this study. However,  $\zeta^0$  gains wavelength dependency at  $d > 4$ , in which case its effect may be detected through *vacuum dispersion* (dependence of the speed of light on wavelength) [25,41,42]. Non-zero values of  $\zeta^1$ ,  $\zeta^2$  and  $\zeta^3$  result in a relative difference in the propagation speed between the two eigenmodes and will therefore alter the polarization state of the observed wave in-flight (*vacuum birefringence*).

### 3. Optical polarimetry

#### 3.1. Monochromatic observations

It is convenient to describe electromagnetic polarization in the Stokes formalism, where each polarization state is uniquely identified by a Stokes vector,  $\mathbf{s} = (q, u, v)$ , where  $q$ ,  $u$  and  $v$  are the intensity normalized Stokes  $Q$ ,  $U$  and  $V$  parameters. The **linear** polarization fraction,  $p$ , and angle,  $\psi$  are then calculated as follows:

$$p = \sqrt{q^2 + u^2} \quad (6)$$

$$\psi = \frac{1}{2} \text{atan2}(u, q) \quad (7)$$

where  $\text{atan2}(y, x)$  is the inverse tangent of  $y/x$  in the appropriate quadrant. Following the IAU convention [43], the frame of reference in the Stokes space is defined such that  $\psi$  is

measured from North due East in ICRS J2000 [44]. The circular polarization fraction is simply  $v$  and may take both positive (anticlockwise<sup>2</sup>) and negative (clockwise) values.

The eigenmodes in Equation (5) are then given by two antiparallel<sup>3</sup> Stokes vectors  $(\zeta^1, \zeta^2, \zeta^3)$  and  $(-\zeta^1, -\zeta^2, -\zeta^3)$ . Both vectors represent the so-called *birefringence axis*, which we denote with  $\boldsymbol{\zeta}$  and, for convenience, take to be positive:

$$\boldsymbol{\zeta} = (\zeta^1, \zeta^2, \zeta^3) \quad (8)$$

The polarization state of a photon (composed of both eigenmodes) propagating in the SME universe,  $\mathbf{s}$  will then precess around the birefringence axis in uniform circular motion with the revolution period of  $\pi/(\omega|\boldsymbol{\zeta}|)$ . The precession direction is against the right hand rule with respect to the birefringence axis. The process is schematically depicted in Fig. 1. Mathematically, the equation of motion is given by:

$$\frac{d\mathbf{s}}{dt} = 2\omega\boldsymbol{\zeta} \times \mathbf{s} = 2\omega \begin{pmatrix} 0 & -\zeta^3 & \zeta^2 \\ \zeta^3 & 0 & -\zeta^1 \\ -\zeta^2 & \zeta^1 & 0 \end{pmatrix} \mathbf{s} \quad (9)$$

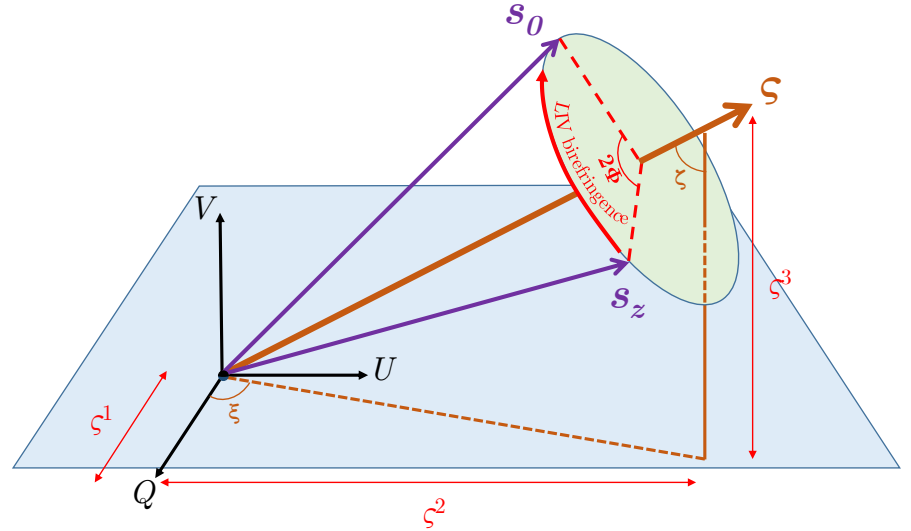


**Figure 1.** Schematic illustration of the LIV effect on the polarization state of a photon in the SME framework. The photon is emitted at the source in some initial polarization state, whose location in the Stokes space (shown here) is indicated with vector  $\mathbf{s}_z$ . In-flight, the state will precess around the birefringence axis  $\boldsymbol{\zeta}$  through angle  $2\Phi$  until, eventually, the photon arrives at the telescope in the state  $\mathbf{s}_0$ . The direction of the birefringence axis and the rate of precession are determined by the particular SME configuration. The blue quadrilateral represents the plane of linear polarization where Stokes  $V$  is 0. Individual components of  $\boldsymbol{\zeta} = (\zeta^1, \zeta^2, \zeta^3)$  and angles referenced in text ( $\zeta, \zeta$ ) are labelled as well.

The Stokes vector represents the polarization state of a photon arriving from a specific direction in the sky and is therefore a function on the celestial sphere, requiring a local reference direction of  $\psi = 0$  (ICRS North according to the IAU convention). Note that  $v$  is

<sup>2</sup> In this work, the terms *clockwise* and *anticlockwise* are taken looking outward such that anticlockwise rotation is due East.

<sup>3</sup> Orthogonal Jones states correspond to antiparallel Stokes states under standard definitions [45].

independent of the choice of reference and  $q \mp iu$  rotate as spin  $\pm 2$  objects<sup>4</sup>. Taking advantage of those symmetries, we re-express  $\mathbf{c}$  and  $\mathbf{s}$  in a spin-weighted basis  $\mathbf{s} = (q - iu, v, q + iu)$  and  $\mathbf{c} = (\zeta^1 - i\zeta^2, \zeta^3, \zeta^1 + i\zeta^2) = (\zeta^+, \zeta^3, \zeta^-)$ , where the spins of vector components are  $+2, 0$  and  $-2$  respectively. The transformation into the new basis may be written as:

$$\hat{S} = \begin{pmatrix} 1 & -i & 0 \\ 0 & 0 & 1 \\ 1 & i & 0 \end{pmatrix} \quad (10)$$

This, in turn, re-organizes the equation of motion, Equation (9), into:

$$\frac{d\mathbf{s}}{dt} = -2i\omega \begin{pmatrix} \zeta^3 & -\zeta^+ & 0 \\ -\zeta^-/2 & 0 & \zeta^+/2 \\ 0 & \zeta^- & -\zeta^3 \end{pmatrix} \mathbf{s} \quad (11)$$

From this point onward, the spin-weighted basis in Equation (11) will be assumed in all vectors and matrices. Denoting the total precession angle from emission to observation of the photon polarization state in Stokes space around the birefringence axis with  $2\Phi$ , the solution to Equation (11) is given by the precession matrix obtained using Rodrigues' formula and transformed into the spin-weighted space:

$$\begin{aligned} \mathbf{s}_0 &= \hat{S} \left[ \hat{S}^{-1} \mathbf{s}_z \cos(2\Phi) - (\hat{S}^{-1} \hat{\zeta} \times \hat{S}^{-1} \mathbf{s}_z) \sin(2\Phi) + \hat{S}^{-1} \hat{\zeta} (\hat{S}^{-1} \hat{\zeta} \cdot \hat{S}^{-1} \mathbf{s}_z) (1 - \cos(2\Phi)) \right] \\ &= \begin{pmatrix} Y^2 & -2ie^{-i\zeta} \sin(\zeta) \sin(\Phi) Y & e^{-2i\zeta} \sin^2(\zeta) \sin^2(\Phi) \\ -ie^{i\zeta} \sin(\zeta) \sin(\Phi) Y & \cos^2(\zeta) + \cos(2\Phi) \sin^2(\zeta) & ie^{-i\zeta} \sin(\zeta) \sin(\Phi) Y^* \\ e^{2i\zeta} \sin^2(\zeta) \sin^2(\Phi) & 2ie^{i\zeta} \sin(\zeta) \sin(\Phi) Y^* & Y^{*2} \end{pmatrix} \mathbf{s}_z \end{aligned} \quad (12)$$

where  $\hat{\zeta}$  is the normalized  $\mathbf{c}$  and the following definitions were introduced:

$$\zeta = \text{atan2}(i(\zeta^+ - \zeta^-), \zeta^+ + \zeta^-) = \arg(\zeta^+) \quad (13)$$

$$\zeta = \text{atan2}(\sqrt{\zeta^+ \zeta^-}, \zeta^3) \quad (14)$$

$$Y = \cos(\Phi) + i \cos(\zeta) \sin(\Phi) \quad (15)$$

The angles  $\zeta$  and  $\zeta$ , in fact, have geometric significance and are labelled in Fig. 1. In Equation (12),  $\mathbf{s}_0 = (q_0 - iu_0, v_0, q_0 + iu_0)$  is the observed Stokes vector of the photon on Earth and  $\mathbf{s}_z = (q_z - iu_z, v_z, q_z + iu_z)$  is the initial Stokes vector at redshift  $z$ .

Considering the precession period of  $\pi/(\omega|\zeta|)$  for the polarization vector, the equation of motion for  $\Phi$  reads:

$$\frac{d\Phi}{dt} = \omega|\zeta| \implies \Phi = \int_0^T \omega|\zeta| dt = \int_0^z \omega_0|\zeta| \frac{dz'}{H_{z'}} \quad (16)$$

where  $T$  is the total time of flight for the photon,  $z$  is the redshift of the source and  $\omega_0$  is the observed angular frequency of the photon at  $z = 0$ . We used  $dt = -dz/[(1+z)H_z]$  and  $\omega(z) = \omega_0(1+z)$ . The Hubble expansion parameter,  $H_z$ , is given by

<sup>4</sup> In this context, a function  $f$  of celestial coordinates (such as  $q, u, v$  or  $q \pm iu$ ) is said to have spin  $s$  if it transforms as  $f \rightarrow f \exp(is\delta\psi)$  when the local North is rotated by  $\delta\psi$  radians due East. In this case,  $q \mp iu \rightarrow (q \mp iu) \exp(\pm 2i\delta\psi)$  and  $v \rightarrow v \exp(i\delta\psi \times 0)$ .

$$H_z = H_0 \left[ \Omega_r(1+z)^4 + \Omega_m(1+z)^3 + \Omega_k(1+z)^2 + \Omega_\Lambda \right]^{1/2} \quad (17)$$

In Equation (17),  $H_0$  is the Hubble constant and  $\Omega_r$ ,  $\Omega_m$ ,  $\Omega_k$  and  $\Omega_\Lambda$  are the present day fractional contributions of radiation, matter, curvature and dark energy to the energy budget of the universe. In this study, we adopt  $H_0 = 67.66 \text{ km s}^{-1} \text{ Mpc}^{-1} = 1.4433 \times 10^{-33} \text{ eV}$ ,  $\Omega_m = 0.3111$ ,  $\Omega_r = 9.182 \times 10^{-5}$ ,  $\Omega_\Lambda = 0.6889$  and  $\Omega_k = 0$ , following [1,46] (see [1] in particular for a discussion of the accuracy of those values in this context and the Hubble tension).

While, in principle, both CPT-even ( $d = 4$ ) and CPT-odd ( $d = 3$ ) contributions to the Lagrangian may exist simultaneously, it is generally preferable to begin the search for Lorentz invariance violation with the smallest number of free parameters. We will follow [1–3,15,25,47] and assume that the effects at a specific  $d$  dominate. Since  $\zeta^3 \propto \omega^{-1} \propto \omega_0^{-1}$  (see Equation 2),  $\Phi$  is wavelength-independent in the  $d = 3$  case. As will be demonstrated shortly, the method proposed in this work draws its constraining power from the frequency dependence of LIV effects, which necessarily restricts the scope of this study to the  $d = 4$  case. However, see alternative approaches in [48–52] to  $d = 3$  searches involving polarimetry of the Cosmic Microwave Background.

For  $d = 4$ , all components of  $k_{AF}^{(3)}$  vanish and, therefore, so does  $\zeta^3$ . Geometrically, the  $d = 4$  case has the birefringence axis,  $\boldsymbol{\zeta}$ , constrained to the plane of linear polarization. For,  $\zeta^3 = 0$ ,  $\zeta$  (Equation 14) evaluates to  $\pi/2$ , allowing the precession formula in Equation (12) to be simplified as follows:

$$\mathbf{s}_0 = \begin{pmatrix} \cos^2(\Phi) & -i \sin(2\Phi)e^{-i\zeta} & \sin^2(\Phi)e^{-2i\zeta} \\ -\frac{i}{2} \sin(2\Phi)e^{i\zeta} & \cos(2\Phi) & \frac{i}{2} \sin(2\Phi)e^{-i\zeta} \\ \sin^2(\Phi)e^{2i\zeta} & i \sin(2\Phi)e^{i\zeta} & \cos^2(\Phi) \end{pmatrix} \mathbf{s}_z \quad (18)$$

### 3.2. Directional dependence

In Equation (18), the dependence of  $\Phi$  on the direction of arrival is determined by the particular SME configuration, which we seek to constrain by comparison with observations. Following [1,15,41], we limit the dependence to 10 linearly independent degrees of freedom (corresponding to the 10 independent components of  $k_F^{(4)}$  setting  $\zeta^\pm$ ) by expanding  $\zeta^\pm$  in terms of  $l = 2$ ,  $s = \pm 2$  spin-weighted spherical harmonics,  ${}_s Y_{l,m}$ , where  $s$ ,  $l$  and  $m$  are the spin, azimuthal and magnetic numbers respectively ( $-2 \leq m \leq 2$ ):

$$\zeta^\pm = \sum_{m=-2}^2 \pm 2 Y_{2,m}(\hat{\mathbf{n}}) (k_{(E)2,m} \pm i k_{(B)2,m}) \quad (19)$$

Here  $\hat{\mathbf{n}}$  is a unit vector pointing in the direction of photon arrival (opposite to the photon momentum) and  $k_{(E,B)jm}$  are complex coefficients of the expansion that obey the following symmetries:

$$k_{(E,B)j,-m} = (-1)^m (k_{(E,B)jm})^* \quad (20)$$

such that there are 10 real independent parameters:  $k_{(E)2,0}$ ,  $k_{(B)2,0}$ ,  $\text{Re}[k_{(E)2,1}]$ ,  $\text{Im}[k_{(E)2,1}]$ ,  $\text{Re}[k_{(E)2,2}]$ ,  $\text{Im}[k_{(E)2,2}]$ ,  $\text{Re}[k_{(B)2,1}]$ ,  $\text{Im}[k_{(B)2,1}]$ ,  $\text{Re}[k_{(B)2,2}]$  and  $\text{Im}[k_{(B)2,2}]$ .

For astronomical tests,  $\hat{\mathbf{n}}$  may be written in some system of celestial coordinates. In this work, we use  $\hat{\mathbf{n}} = (\alpha, \delta)$ , where  $\alpha$  and  $\delta$  are the J2000 ICRS [44] right ascension and declination<sup>5</sup>.

Substituting Equation (19) in Equation (16):

$$\Phi = \omega_0 \left| \sum_{m=-2}^2 {}_2Y_{2,m}(\hat{\mathbf{n}})(k_{(E)2,m} + ik_{(B)2,m}) \right| \int_0^z \frac{dz'}{H_{z'}} \quad (21)$$

### 3.3. Broadband observations

Astronomical observations of the Stokes parameters  $q_0$ ,  $u_0$  and  $v_0$  are taken over some finite band defined by a dimensionless detection efficiency  $\tau(\omega_0)$ , rather than a single monochromatic frequency. The observed effective Stokes parameter,  $Q_0$ , is then determined by the weighted average of the observed Stokes parameter  $q_0$ :

$$Q_0 = \frac{\int_0^\infty \tau(\omega_0) q_0(\omega_0) d\omega_0}{\int_0^\infty \tau(\omega_0) d\omega_0} = \mathcal{T}[q_0] \quad (22)$$

where we defined the operator  $\mathcal{T}$  as the efficiency-weighted average. The other two Stokes parameters are then  $U_0 = \mathcal{T}[u_0]$  and  $V_0 = \mathcal{T}[v_0]$ . Observed broadband linear polarization fraction ( $\Pi_0$ ) and angle ( $\Psi_0$ ) may then be defined equivalently to Equations (6) and (7):

$$\Pi_0 = \sqrt{Q_0^2 + U_0^2} \quad (23)$$

$$\Psi_0 = \frac{1}{2} \text{atan2}(U_0, Q_0) \quad (24)$$

For convenience, we introduce a primed system of Stokes coordinates, rotated with respect to the ICRS J2000 coordinates anticlockwise through  $\xi$ :

$$\mathbf{s}' = \begin{pmatrix} q' - iu' \\ v' \\ q' + iu' \end{pmatrix} = \begin{pmatrix} e^{i\xi} & 0 & 0 \\ 0 & 1 & 0 \\ 0 & 0 & e^{-i\xi} \end{pmatrix} \begin{pmatrix} q - iu \\ v \\ q + iu \end{pmatrix} \quad (25)$$

As a result of this rotation, the polarization angle decreases by  $\xi/2$ , while both linear and circular polarization fractions remain unchanged. In primed coordinates, the observed broadband Stokes parameters can be expressed in simple forms by assuming that the source polarization spectrum only slowly varies with  $\omega$  across the optical range, implying that  $\mathbf{s}_z(\omega_z) \approx \mathbf{s}_z$ . This assumption is justifiable by low redshift (i.e. SME-free) spectropolarimetry [2] that shows weak dependence of polarization on wavelength for most galaxies due to the optical range being comparatively narrow.  $Q_0$ ,  $U_0$ , and  $V_0$  are then related to the Stokes parameters at the source as:

$$Q'_0 = q'_z \quad (26)$$

$$U'_0 = +u'_z \mathcal{T}[\cos(2\Phi)] + v'_z \mathcal{T}[\sin(2\Phi)] \quad (27)$$

$$V'_0 = -u'_z \mathcal{T}[\sin(2\Phi)] + v'_z \mathcal{T}[\cos(2\Phi)] \quad (28)$$

Note that the functional forms of  $\mathcal{T}[\cos(2\Phi)]$  and  $\mathcal{T}[\sin(2\Phi)]$  are entirely determined by the instrument and may be pre-tabulated for a range of  $\Phi$  values for fast lookup. Equations

<sup>5</sup> Note that spherical harmonics are most commonly written in traditional spherical polar coordinates  $(\phi, \theta)$ , where  $\theta$  is the polar angle which corresponds to  $(\pi/2 - \delta)$  (so-called *codeclination*) and  $\phi = \alpha$  given an appropriate prime meridian.



(26, 27, 28) demonstrate that the total polarization fraction ( $\sqrt{q^2 + u^2 + v^2}$ ) is conserved in the monochromatic limit ( $\mathcal{T}[x] \rightarrow x$ ); however, it will in general decrease with redshift for broadband observations due to the polarization washout induced by the frequency dependence of  $d = 4$  SME effects (i.e.  $|\mathcal{T}[x]| < |x|$ ). This effect is illustrated in Fig. 2, displaying the value of  $\mathcal{T}[\sin(2\Phi)]$  as a function of  $\Phi$  for the cases of monochromatic, filtered broadband and unfiltered broadband observations. While the amplitude of the operand is conserved in the monochromatic case, it decays in both broadband cases with the unfiltered decay being more rapid due to a wider range of wavelengths observed.

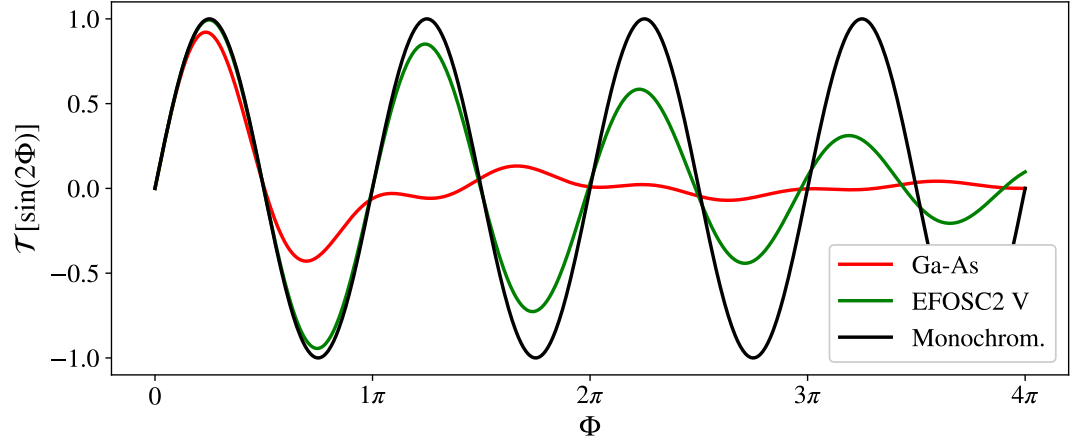


**Figure 2.** Effect of observing SME birefringence through a broad detection efficiency band. The curves show the effect of the broadband operator  $\mathcal{T}[x]$  on the amount of LIV-induced linear polarization in-flight (see Equations 27 and 28) as a function of  $\Phi$  (see Fig. 1). The three cases shown correspond to a monochromatic observation (black,  $\mathcal{T}[\sin(2\Phi)] \rightarrow \sin(2\Phi)$ ), a broadband observation with an unfiltered Ga-As photomultiplier tube (red) and a broadband observation in the V-band of the EFOSC2 [53] instrument (green). This simulation assumes observations at zenith. See section 5 for more details on instruments, bands and atmospheric effects.

### 3.4. Likelihood model

To differentiate SME predictions for the observed broadband polarization parameters ( $Q_0, U_0, V_0, \Psi_0$  and  $\Pi_0$ ) derived above from the actual experimental measurements, we introduce subscript  $m$  for the latter, such that in the case of the chosen SME configuration being a perfect description of LIV we must have  $Q_0 = Q_m, U_0 = U_m$  etc. in the absence of other effects.

In the limit of weak SME motivated by strict constraints established in previous work [1–3], we expect the change in Stokes parameters due to SME to be small such that the overall ratio of linear to circular polarization ( $\Pi/V$ ) for extragalactic photons is only mildly perturbed in-flight. Since both experimental and theoretical considerations (e.g. [54–57]) suggest that linearly polarized emission dominates over circularly polarized emission for nearly all realistic extragalactic sources, we further assume that  $|v_z| \ll p_z$  and  $|V_0| \ll \Pi_0$ . Under this assumption, Equations (27) and (28) suggest that the overall effect of the SME is to suppress linear polarization and enhance circular polarization in-flight, as demonstrated in Fig. 3b where linear and circular polarization fractions are plotted on the same set of axes as functions of redshift. Therefore, SME configurations are ruled out by measurements of lower  $|V_m|$  and higher  $\Pi_m$ . In the extreme case, an error-free measurement of  $V_m = 0$  or  $\Pi_m = 1$  would entirely rule out all SME configurations considered in this study.

Assuming that the source polarization is somehow known (see section 4), Equations (26, 27, 28) can be used to predict the expected observed polarization for any  $d = 4$  SME

configuration and for any instrument (encoded in the functional form of  $\mathcal{T}$ ). The prediction must then be compared to experimental results, which may be accomplished by evaluating the likelihood of compatibility of the observed data with theory. For broadband polarimetry, three types of measurements are available:

- Linear polarization fraction,  $\Pi_m$ .
- Polarization angle,  $\Psi_m$ .
- Circular polarization fraction,  $V_m$ .

In our method, we advocate deriving constraints on SME parameters from the linear and circular polarization fraction measurements,  $\Pi_m$  and  $V_m$ . The polarization angle,  $\Psi_m$ , is still essential in the method (section 4), but will not be used in the likelihood model directly.

Since the measured circular polarization,  $V_m$ , may take both positive and negative values, we assume a Gaussian parent distribution with the mean of  $V_m$  and the standard deviation of  $\sigma_V$ . The likelihood of compatibility of such a measurement with the SME prediction  $V_0$  may be written as follows:

$$\mathcal{P}_{\text{circ}} = \begin{cases} \int_{V_0}^{\infty} \frac{1}{\sigma_V \sqrt{2\pi}} \exp\left(-\frac{(V-V_m)^2}{2\sigma_V^2}\right) dV, & \text{if } V_0 > 0 \\ \int_{-\infty}^{V_0} \frac{1}{\sigma_V \sqrt{2\pi}} \exp\left(-\frac{(V-V_m)^2}{2\sigma_V^2}\right) dV, & \text{if } V_0 < 0 \end{cases} \quad (29)$$

A particular SME configuration is rejected if the observed circular polarization fraction is lower than predicted in absolute value ( $V_m < V_0$  for  $V_0 > 0$ ,  $V_m > V_0$  for  $V_0 < 0$ ).

The measured linear polarization degree,  $\Pi_m$ , may display strongly non-Gaussian behavior due to being an intrinsically positive quantity. We assume  $\Pi_m$  to be drawn from the Rice distribution ( $P(\Pi|\hat{\Pi})$ , Equation A5) with  $\hat{\Pi} = \Pi_m$  and  $\text{Var}[\Pi] = \sigma_{\Pi}^2$ , where  $\sigma_{\Pi}$  is the uncertainty of the measurement and  $\text{Var}[\Pi]$  is given in Equation (A7). The statistical distribution of linear polarization fraction and the bias in linear polarization measurements are discussed in appendix A.

Since the overall SME effect is to decrease linear polarization, a particular SME configuration is rejected if the observed polarization degree is larger than expected ( $\Pi_m > \Pi_0$ ). Therefore, the probability of compatibility with SME prediction  $\Pi_0$  may be written as follows:

$$\mathcal{P}_{\text{lin}} = \int_0^{\Pi_0} P(\Pi|\Pi_m) dp \quad (30)$$

The total compatibility of a given dataset of both circular and linear polarimetry is obtained by multiplying all individual likelihoods together:

$$\mathcal{P} = \prod_i \mathcal{P}_{\text{circ}}^{(i)} \mathcal{P}_{\text{lin}}^{(i)} \quad (31)$$

where the product is taken over all measured sources. The constraints on the 10 independent SME parameters are derived by maximizing the likelihood with respect to them and extracting the standard errors, as detailed in section 6.

#### 4. Source parameters

The likelihood model introduced in the previous section requires some assumption of the photon polarization state at the source,  $\mathbf{s}_z$ . In this section, we introduce our assumptions for the polarization angle and linear and circular polarization fractions at the source:  $\psi_z$ ,  $p_z$  and  $v_z$ . In general, we aim to choose the most conservative values, i.e. values for which fewest SME configurations are rejected or, alternatively, values that maximize the compatibility likelihood  $\mathcal{P}$ .

#### 4.1. Circular polarization

For all observed astronomical sources, we assume the circular polarization at the source to be zero ( $v_z = 0$ ). This assumption is justified by both experimental and theoretical studies in literature [54–57] finding negligible or very small circular polarization for the majority of extragalactic sources. For sources with small but non-negligible circular polarization ( $0 < |v_z| \ll p_z$ ), the assumption of  $v_z = 0$  remains conservative, since non-zero  $v_z$  results in an increase in the magnitude of observed circular polarization (Equation 28) and, therefore, weaker constraints on SME coefficients (larger  $\mathcal{P}_{\text{circ}}$ ).

#### 4.2. Linear polarization

In our previous work [1–3], large values of  $p_z$  were adopted as most conservative since  $\mathcal{P}_{\text{lin}}$  increases with  $p_z$  in the limit of weak SME (small  $\Phi$ ) and dominance of linear polarization over circular ( $|v_z| \ll p_z$ ). Specifically, the most conservative assumption for the value of  $p_z$  was taken as the largest possible source polarization fraction. For example, [2,3] adopted  $p_z = 1.0$  for all sources ignoring astrophysical considerations, while [1] adopted  $p_z = 0.7$  based on literature polarimetry of low redshift sources, resulting in somewhat stricter constraints on SME parameters.

However, previous work disregarded the fact that  $\mathcal{P}_{\text{circ}}$ , in general, decreases with  $p_z$  since larger linear polarization at the source results in faster conversion of linear to circular polarization in-flight and, hence, larger observed circular polarization  $V_0$ . Therefore, the assumption of large  $p_z$  may not be most conservative in some instances when circular polarimetry is available. An example of this effect is demonstrated in Fig. 3a. In the figure, the values of  $\mathcal{P}_{\text{lin}}$ ,  $\mathcal{P}_{\text{circ}}$  and the total compatibility  $\mathcal{P}$  are shown for a test observation and a test SME configuration as a function of the assumed source polarization  $p_z$ .  $\mathcal{P}_{\text{lin}}$  increases with  $p_z$  monotonically with an asymptote at  $\mathcal{P}_{\text{lin}} = 1$ , suggesting higher values of  $p_z$  as most conservative in the absence of other considerations. On the other hand,  $\mathcal{P}_{\text{circ}}$  decreases with  $p_z$  monotonically. Therefore, a more conservative assumption for  $p_z$  is one that maximizes the total compatibility, which in this example falls around  $p_z = 0.55$ .

In this study, we determine the most conservative value of  $p_z$  by numerically maximizing the total likelihood of compatibility,  $\mathcal{P}_{\text{lin}}\mathcal{P}_{\text{circ}}$ , for each available polarization measurement.

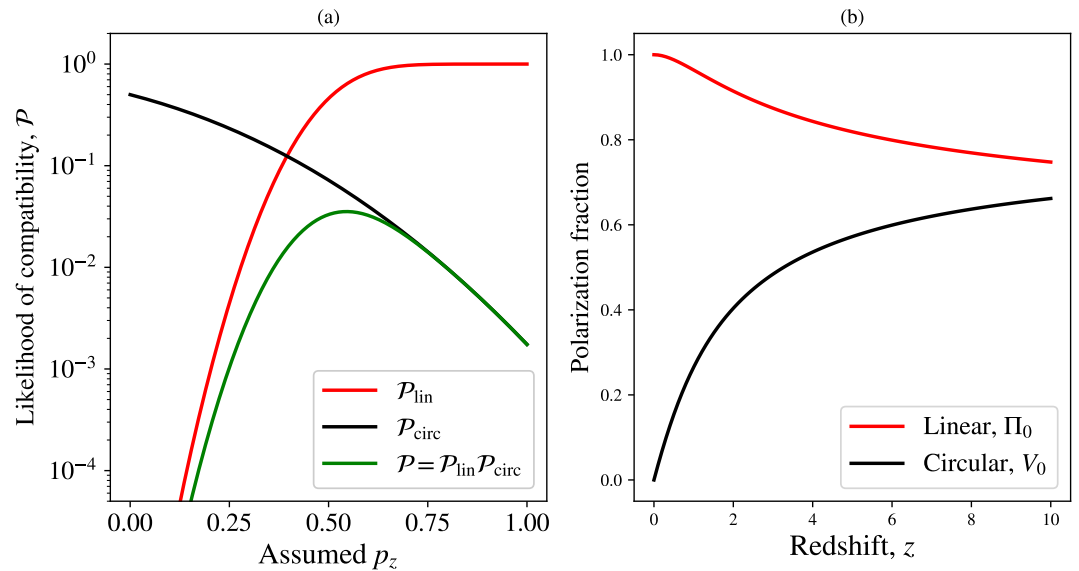


**Figure 3.** (a) Plots of linear, circular and total likelihood of compatibility for a single test measurement as a function of the assumed polarization fraction at the source. The astrophysical source is assumed to be located at the Vernal equinox ( $\alpha = 0, \delta = 0$ ) and  $z = 2.0$ . For demonstration purposes, the adopted test measurement is  $\Pi_m = 0.5 \pm 0.1$ ,  $V_m = 0.0 \pm 0.01$  and  $\Psi_m = 0.0$ . The adopted SME configuration has all ten parameters considered in this study set to  $10^{-34}$  (the order of magnitude of the upper limit derived in [1,3]). The test measurement is assumed to have been taken through the EFOSC2 [53] V filter in zenith (see section 5). Note that the linear compatibility increases while the circular compatibility decreases with  $p_z$ . The most conservative assumption for the value of  $p_z$  is the one maximizing the total compatibility, which in this case occurs around  $p_z = 0.55$ . (b) The effect of SME on linear and circular polarization fractions, shown here as  $\Pi_0$  and  $V_0$  as functions of the redshift of the source. The predictions shown here were derived for a test source at the Vernal equinox ( $\alpha = 0, \delta = 0$ ) observed through the EFOSC2 [53] V filter in zenith. The initial polarization state of the photons is assumed to be  $v_z = 0, p_z = 1$  and  $\psi_z = -30^\circ$ . The adopted SME configuration is the same as in (a).

#### 4.3. Polarization angle

The polarization angle at the source,  $\psi_z$ , may be estimated by seeking a value that reproduces the observed polarization angle,  $\Psi_0 = \Psi_m$ , under the most conservative assumptions for  $p_z$  and  $v_z$  as described above. Combining Equations (26,27,28) and solving for  $\psi_z$ :

$$\psi_z = \psi'_z + \frac{\xi}{2} = \frac{1}{2} \text{atan2} \left( \frac{U'_m}{\mathcal{T}[\cos(2\Phi)]}, Q'_m \right) + \frac{\xi}{2} \quad (32)$$

where  $Q'_m = \Pi'_m \cos(2\Psi'_m)$ ,  $U'_m = \Pi'_m \sin(2\Psi'_m)$  and  $\Psi'_m = \Psi_m - \xi/2$ . As in [1,3], the uncertainty in  $\Psi_m$  is not required by the method.

### 5. Sample dataset

We derive constraints on the 10 real SME parameters by maximizing the total likelihood of compatibility (Equation 31) for a set of linear and circular polarimetric measurements from literature. The dataset used in this study includes 21 quasars and was adopted from the compilation of archival linear polarimetry and original circular polarimetry in [58]. All data used in this analysis are reproduced in Table 1.

Circular polarization measurements in [58] were obtained through the Bessel  $V$  filter (ESO #641) using the EFOSC2 [53] instrument mounted on the ESO 3.6 m telescope at La Silla Observatory.

The linear polarization measurements for the same sources were compiled by [58] from seven references that we refer to as Impey+1990 [59], Berriman+1990 [60], Hutsemékers+1998 [61], Visvanathan+1998 [62], Schmidt+1999 [63], Lamy+2000 [64] and Sluse+2005 [65].

The measurements from Impey+1990 [59] were obtained with an unfiltered Ga-As photomultiplier tube in the MINIPOL polarimeter mounted on the Irénée du Pont 100 inch telescope at Las Campanas Observatory. The measurements from Berriman+1990 [60] were obtained with an unfiltered Ga-As photomultiplier in the Two-Holer polarimeter/photometer mounted on the Bok 2.3 m telescope at Steward Observatory and the 1.5 m telescope at Mount Lemmon Observing Facility. The measurements from Schmidt+1999 [63] were obtained unfiltered using polarimeters mounted on the Bok 2.3 m telescope at Steward Observatory. The publication does not specify the detector; however, it is mentioned that the waveband and sensitivity were very similar to the Breger polarimeter [66] at McDonald Observatory. Since [66] employ the response curve of a Ga-As photomultiplier tube in their analysis, we assume that the Steward Observatory polarimeters used some type of Ga-As tubes as well. The measurements from Visvanathan+1998 [62] were obtained with an unfiltered Na-K-Cs-Sb (S20) photomultiplier in an automated polarimeter [67] mounted on the Anglo-Australian Telescope at Siding Spring Observatory. The measurements from Hutsemékers+1998 [61], Lamy+2000 [64] and Sluse+2005 [65] were obtained through the Bessel  $V$  filter using the EFOSC1/EFOSC2 [53] instrument at La Silla Observatory, which we assume to have sufficiently similar transmission profile to the Bessel  $V$  filter (ESO #641) used by [58] for circular polarimetry.

### 5.1. Detection efficiency profiles

Our method requires efficiency profiles,  $\tau(\omega_0)$ , for each measurement in the dataset. For filtered observations, the transmission profile of the filter is typically self-sufficient with atmospheric transmission, detector response, mirror reflectivity etc. only contributing minor higher order corrections. For unfiltered observations, the response curve of the detector becomes most determining with the atmospheric transmission making a significant contribution at the blue end of the visible spectrum where the ozone layer predominantly sets the short wavelength cut-off of the instrument.

**Table 1.** Coordinates, redshifts, and optical linear/circular polarization measurements of the selected quasars. References (z Ref.) are provided for the redshift values. Transmission bands and references (p Ref.) are provided for the linear polarization measurements. All circular polarization measurements were taken through the Bessel V filter and were reported in [58]. The detection efficiency profiles for the Bessel V filter, Ga-As photomultiplier, and Na-K-Cs-Sb (S20) photomultiplier are shown in Figure 4.

Object Identifier	RAJ2000 ( $\alpha$ )	DEJ2000 ( $\delta$ )	z	z Ref.	$\Pi_m$ (%)	$\Psi_m$ ( $^\circ$ )	Band	p Ref.	$V_m$ (%)
QSO B1120+0154	11 23 20.73	+01 37 47.5	1.47	[68]	1.95 $\pm$ 0.27	9 $\pm$ 4	V	[61]	-0.02 $\pm$ 0.05
QSO B1124-186	11 27 04.39	-18 57 17.4	1.05	[69]	11.68 $\pm$ 0.36	37 $\pm$ 1	V	[65]	-0.04 $\pm$ 0.08
QSO J1130-1449	11 30 07.05	-14 49 27.4	1.19	[70]	1.30 $\pm$ 0.40	23 $\pm$ 10	Ga-As	[59]	-0.05 $\pm$ 0.05
QSO B1157+014	11 59 44.83	+01 12 07.0	2.00	[71]	0.76 $\pm$ 0.18	39 $\pm$ 7	V	[64]	-0.10 $\pm$ 0.08
LBQS 1205+1436	12 08 25.38	+14 19 21.1	1.64	[68]	0.83 $\pm$ 0.18	161 $\pm$ 6	V	[64]	-0.10 $\pm$ 0.09
LBQS 1212+1445	12 14 40.27	+14 28 59.3	1.63	[72]	1.45 $\pm$ 0.30	24 $\pm$ 6	V	[61]	0.15 $\pm$ 0.09
QSO B1215-002	12 17 58.73	-00 29 46.3	0.42	[72]	23.94 $\pm$ 0.70	91 $\pm$ 1	V	[65]	-0.42 $\pm$ 0.40
QSO B1216-010	12 18 34.93	-01 19 54.3	0.554	[73]	11.20 $\pm$ 0.17	100 $\pm$ 1	V	[65]	-0.01 $\pm$ 0.07
Ton 1530	12 25 27.40	+22 35 13.0	2.05	[74]	0.92 $\pm$ 0.14	169 $\pm$ 4	V	[65]	0.01 $\pm$ 0.10
QSO J1246-2547	12 46 46.80	-25 47 49.3	0.63	[69]	8.40 $\pm$ 0.20	110 $\pm$ 1	Ga-As	[59]	-0.23 $\pm$ 0.20
QSO B1246-0542	12 49 13.86	-05 59 19.1	2.23	[71]	1.96 $\pm$ 0.18	149 $\pm$ 3	Ga-As	[63]	0.01 $\pm$ 0.03
QSO B1254+0443	12 56 59.92	+04 27 34.4	1.02	[72]	1.22 $\pm$ 0.15	165 $\pm$ 3	Ga-As	[60]	-0.02 $\pm$ 0.04
QSO B1256-229	12 59 08.46	-23 10 38.7	0.481	[75]	22.32 $\pm$ 0.15	157 $\pm$ 1	V	[65]	0.18 $\pm$ 0.04
QSO J1311-0552	13 11 36.56	-05 52 38.6	2.19	[76]	0.78 $\pm$ 0.28	179 $\pm$ 11	V	[61]	-0.08 $\pm$ 0.06
LBQS 1331-0108	13 34 28.06	-01 23 49.0	1.78	[72]	1.88 $\pm$ 0.31	29 $\pm$ 5	V	[61]	-0.04 $\pm$ 0.06
[VV96] J134204.4-181801	13 42 04.41	-18 18 02.6	2.21	[76]	0.83 $\pm$ 0.15	20 $\pm$ 5	V	[65]	-0.01 $\pm$ 0.07
2E 3238	14 19 03.82	-13 10 44.8	0.13	[77]	1.63 $\pm$ 0.15	44 $\pm$ 3	Ga-As	[61]	0.05 $\pm$ 0.06
LBQS 1429-0053	14 32 29.25	-01 06 16.1	2.08	[72]	1.00 $\pm$ 0.29	9 $\pm$ 9	V	[61]	0.02 $\pm$ 0.08
QSO J2123+0535	21 23 44.52	+05 35 22.1	1.88	[78]	10.70 $\pm$ 2.90	68 $\pm$ 6	Ga-As	[59]	0.02 $\pm$ 0.15
QSO B2128-123	21 31 35.26	-12 07 04.8	0.50	[71]	1.90 $\pm$ 0.40	64 $\pm$ 6	S20	[62]	-0.04 $\pm$ 0.03
QSO B2155-152	21 58 06.28	-15 01 09.3	0.67	[69]	22.60 $\pm$ 1.10	7 $\pm$ 2	Ga-As	[59]	-0.35 $\pm$ 0.10

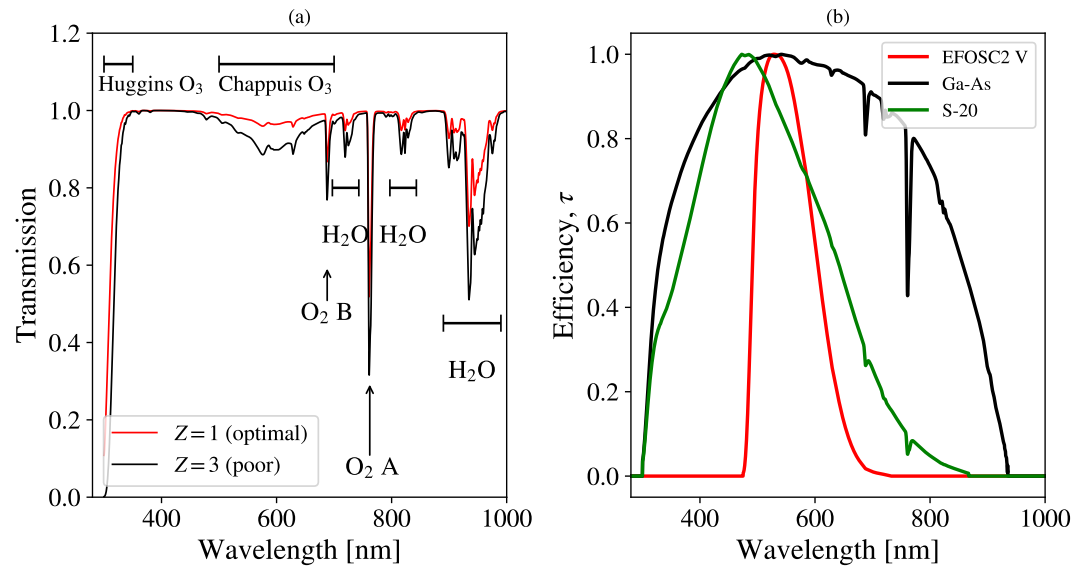


**Figure 4.** (a) Atmospheric transmission model employed in this study as a function of wavelength for two airmasses:  $Z = 1, 3$ . Most prominent absorption features due to ozone ( $O_3$ ), oxygen ( $O_2$ ) and water vapour ( $H_2O$ ) are labelled. For clarity, the plots exclude Rayleigh and Mie scattering effects (however, they are included in the analysis). (b) Detection efficiency profiles of the three instruments relevant to this study. For the  $V$  band, the transmission of the filter is shown. For both Ga-As and S-20 photomultipliers, the response curves of the detector are used instead. All curves are corrected for the atmospheric transmission. In the figure, the  $Z = 1$  atmosphere was applied.

For all filtered observations through the Bessel  $V$  band, we adopt the ESO #641 transmission profile available online<sup>6</sup>. For unfiltered observations, we take generic response curves of the corresponding photomultiplier tubes (Ga-As and S20) from [79, p.101]. All profiles are multiplied by atmospheric transmission, based on the atmospheric radiation model in [80] calculated for the geographic altitude of 2400 m and weather conditions of Cerro Paranal. The model employs the radiative transfer routine in [81] and HITRAN opacity database [82]. The altitude and conditions adopted by the model are generally similar to those at the majority of aforementioned facilities contributing data to this study.

Since the atmospheric transmission strongly depends on the target elevation above the horizon, we carry out all calculations for the cases of both optimal (airmass<sup>7</sup>  $Z = 1.0$ ) and poor (airmass  $Z = 3.0$ ) conditions. The final efficiency profiles used in both cases are provided in Fig. 4. All profiles are normalized to  $\tau = 1$  at the peak efficiency for convenience, since our method is not sensitive to multiplicative pre-factors, as evident from Equation (22).

## 6. SME constraints

Following [1,3], we explore the ten-dimensional likelihood distribution given by Equation (31) using Metropolis-Hastings Markov-Chain Monte Carlo (MCMC) approach. Exploration is carried out by so-called *walkers* that spawn at some location in the likelihood space (i.e. some combination of SME parameters) and proceed in random Monte Carlo steps. In each step, offsets for the positions of the walkers are drawn from a suitable proposal distribution in all ten dimensions and the likelihood of compatibility at the new location is estimated. The ratio of the new likelihood to the old one is then compared to a uniform random number between

<sup>6</sup> <https://www.eso.org/sci/facilities/lasilla/instruments/efosc/inst/Efosc2Filters.html>

<sup>7</sup> In this analysis, we define the airmass,  $Z$ , as the integrated atmospheric density along the line of sight to the source normalized to  $Z = 1$  in zenith.

0 and 1 and the step is accepted if the former exceeds the latter. The non-zero probability of stepping into lower likelihood is implemented to prevent walkers from getting “stuck” in local minima if any happen to be present in the likelihood space. The probability distribution for each of the SME parameters is then extracted by assuming the probability of each value along a given dimension to be proportional to the number of steps that the walkers spent in its immediate proximity.

**Table 2.** Derived constraints on the values of the 10 real  $d = 4$  SME parameters. The upper and lower bounds were taken as the 5th and 95th percentiles of the distributions shown in Fig. 5. For each parameter, the most conservative of the  $Z = 1$  and  $Z = 3$  cases is shown.

SME Parameter	Upper bound ( $\times 10^{-35}$ )	Lower bound ( $\times 10^{-35}$ )
$k_{(E)2,0}$	$\leq 2.9$	$\geq -1.2$
Re $\left[ k_{(E)2,1} \right]$	$\leq 1.8$	$\geq -1.5$
Im $\left[ k_{(E)2,1} \right]$	$\leq 0.2$	$\geq -1.4$
Re $\left[ k_{(E)2,2} \right]$	$\leq 3.0$	$\geq -1.7$
Im $\left[ k_{(E)2,2} \right]$	$\leq 1.4$	$\geq -1.4$
$k_{(B)2,0}$	$\leq 3.2$	$\geq -0.7$
Re $\left[ k_{(B)2,1} \right]$	$\leq 1.3$	$\geq -1.8$
Im $\left[ k_{(B)2,1} \right]$	$\leq 1.9$	$\geq -0.8$
Re $\left[ k_{(B)2,2} \right]$	$\leq 2.1$	$\geq -2.1$
Im $\left[ k_{(B)2,2} \right]$	$\leq 1.2$	$\geq -2.3$

In this study, we followed [1,3] and used a Gaussian proposal distribution with the same standard deviation in all dimensions. The standard deviation was chosen by first assuming all SME parameters to be equal and searching a value where the likelihood evaluates to the midpoint between the extreme cases of infinitely strong ( $k_{(E,B)l,m} \rightarrow \infty$ ) and infinitely weak ( $k_{(E,B)l,m} \rightarrow 0$ ) SME. The result,  $\sim 2 \times 10^{-36}$ , is expected to be of comparable magnitude to the average width of the likelihood distribution across all dimensions. The initial positions for 20 MCMC walkers were drawn from the proposal distribution as well. The run was terminated when each walker completed 500 steps (accepted or rejected) for the total of  $10^4$  steps across all walkers. At the end of the chain, the step acceptance ratios were found to be 0.21 and 0.23 for the  $Z = 1$  and  $Z = 3$  cases. The extracted probability distributions for all 10 SME parameters are given in Fig. 5. The constraints on individual parameters (upper and lower bounds) were taken as the 5th and 95th percentiles of the corresponding distributions. The numeric values are summarized in Table 2. In the case of differing results for the  $Z = 1$  and  $Z = 3$  cases, the most conservative case was taken (i.e. minimum value for the lower bound and maximum value for the upper bound).



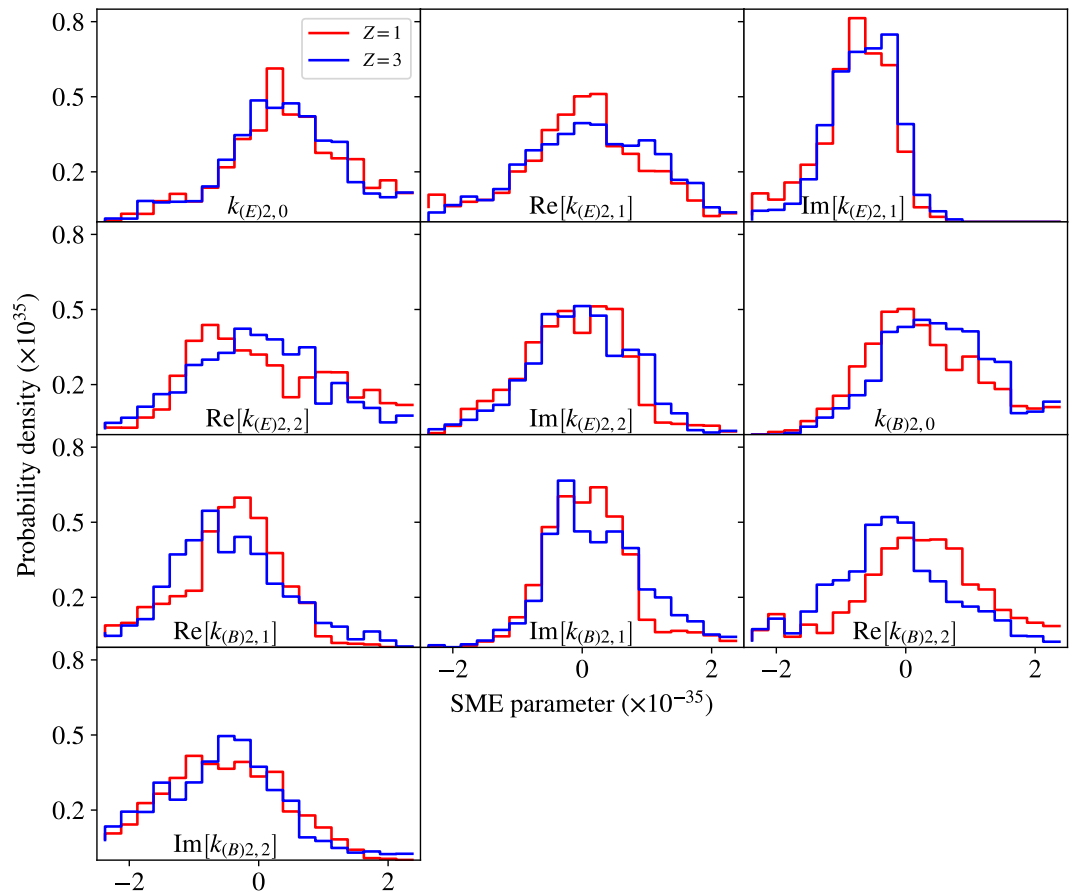


**Figure 5.** Probability distributions for the values of the 10 real  $d = 4$  SME parameters extracted from MCMC chains for the dataset of optical circular and linear polarimetry considered in this study. All parameters are dimensionless. Color-coded are the cases of  $Z = 1$  (red) and  $Z = 3$  (blue) atmospheres (section 5). The distributions are uniformly binned with the bin width of  $2.5 \times 10^{-36}$  for the total of 20 bins.

## 7. Conclusion

In this work we used optical circular and linear polarimetry of high redshift extragalactic sources to derive new constraints on the Lorentz invariance violation in the framework of the Standard-Model Extension at mass dimension  $d = 4$ . The numerical values of the constraints are expressed as upper and lower bounds on the 10 SME parameters summarized in Table 2. The detailed probability distributions for each parameter have also been calculated and are presented in Fig. 5. Since the exact conditions of the literature observations employed in this study are unknown, all calculations have been carried out for two different airmasses ( $Z = 1$  and  $Z = 3$ ) with no noticeable difference in results.

Similarly to [1,3], we find the probability distributions for individual SME parameters (Fig. 5) consistent with zero within two sigma. Unlike [1,3], our results display more asymmetry around the origin with the most notable example being  $\text{Im}[k_{(E)2,1}]$  which appears heavily skewed towards negative values. We note that circular polarimetry is generally expected to be more sensitive to the sign of coefficients than linear polarimetry due to the fact that both clockwise and anticlockwise circular polarization may be induced by the SME. The observed asymmetry in the distribution is likely caused by the particular combination of clock-

wise/anticlockwise circular polarization measurements along the lines of sight considered in the sample dataset.

The discussion of systematic errors in [1] is mostly applicable to this study as well. In our method, it is assumed that any drift in the photon polarization state between the source and the telescope is induced by the LIV and not by astrophysical processes. We first note that any process that reduces linear or enhances circular polarization would weaken our constraints due to the conservative likelihood model used. While modelling such effects may improve the derived constraints further, we are at no risk of falsely ruling out viable SME configurations. If unaccounted, said astrophysical processes may eventually establish a lower bound on parameter constraints derivable using our method. Given the considerable improvement of the constraints derived in this study compared to its predecessors (see below), it is reasonable to assume that such lower bound has not yet been reached.

On the other hand, astrophysical processes that enhance linear or reduce circular polarization are of much greater concern as they would falsely tighten our constraints on SME effects. Fortunately, very few of such processes are known to occur in the optical regime and most are expected to average out over multiple lines of sight. A prominent example of such effect includes polarization and de-polarization of radiation by the interstellar medium [83,84].

Our constraints are directly comparable to those derived in [1] and [3] and are tighter than both by approximately an order of magnitude due to our use of circular polarimetry which has not been applied in similar studies before. We note further that this result has been achieved with only 21 unique lines of sight, which is less than the dataset in [3] containing 27 lines of sight and much less than the dataset in [1] containing 1278 lines of sight. Our analysis demonstrates that deriving constraints from circular and linear polarimetry simultaneously is a more efficient method than the ones previously employed in literature as not only does it provide better constraints for fewer sources, but is also free of the somewhat arbitrary assumption of excessively high initial linear polarization fraction. We expect that a larger sample size as well as higher quality circular polarimetry may significantly improve the constraints derived in this work. Unfortunately, the scarcity of circular measurements for extragalactic sources, in part due to their characteristically weak signal, imposes strict limits on the maximum improvement one may expect from archival data and calls for new optical polarization surveys. Additionally, the process of estimating the initial linear polarization at the source,  $p_z$ , through numerical optimization is far more computationally demanding than the methods in [1,3], limiting the number of MCMC steps used in this study ( $10^4$  compared to  $0.5 \times 10^6$  in [1] and  $10^7$  in [3]) and potentially requiring high performance computing for adequate processing of a larger dataset in the future.

**Author Contributions:** RG led the analysis of linear and circular polarization data. PB collected the dataset of linear and circular polarization data, filter transmission curves and PMT efficiencies. FK co-developed the analysis method.

**Funding:** FK acknowledges NASA support under grant 80NSSC18K0264.

**Acknowledgments:** The authors would like to thank Alan Kostelecký, Matthew Mewes, David Mattingly, Henric Krawczynski, Jim Buckley, Floyd Stecker, and Brian Keating for fruitful discussions. We are grateful to the late Andy Friedman without whom this collaboration would never have happened. This work made use of the SIMBAD database, operated at CDS, Strasbourg, France.

## Appendix A. Polarization statistics

In this appendix we present our treatment of the linear polarization degree distribution and the linear polarization bias. Assuming no variability in the source, there exists some “true”

linear polarization degree,  $\hat{p}$ , which is related to the “true” intensity-normalized Stokes  $\hat{q}$  and  $\hat{u}$  parameters:

$$\hat{p} = \sqrt{\hat{q}^2 + \hat{u}^2} \quad (\text{A1})$$

We assume the measured Stokes parameters,  $q$  and  $u$ , to be normally distributed around their “true” counterparts,  $\hat{q}$  and  $\hat{u}$ , with identical standard deviations of  $\sigma$ . Furthermore, we assume no correlation between  $q$  and  $u$ . The probability density of observing a particular pair of  $q$  and  $u$  is then a product of their respective Gaussian distributions:

$$P(q, u | \hat{q}, \hat{u}) = \frac{1}{2\pi\sigma^2} \exp\left(-\frac{(q - \hat{q})^2}{2\sigma^2}\right) \exp\left(-\frac{(u - \hat{u})^2}{2\sigma^2}\right) \quad (\text{A2})$$

Equivalently, in polar coordinates:

$$P(p, \psi | \hat{p}, \hat{\psi}) = \frac{p}{\pi\sigma^2} \exp\left(-\frac{1}{2\sigma^2} [p^2 + \hat{p}^2 - 2p\hat{p} \cos(2\psi - 2\hat{\psi})]\right) \quad (\text{A3})$$

where we substituted  $q = p \cos(2\psi)$ ,  $u = p \sin(2\psi)$  and their “true” counterparts. Note the added pre-factor of  $2p$  due to the coordinate transformation,  $dqdu = 2pdpd\psi$ . Now integrate Equation (A3) over all  $\psi$  to obtain the distribution of  $p$  independently of  $\psi$ :

$$P(p | \hat{p}) = \int_0^\pi P(p, \psi | \hat{p}, \hat{\psi}) dp d\psi = \frac{p}{\sigma^2} \exp\left(-\frac{p^2 + \hat{p}^2}{2\sigma^2}\right) I_0\left(\frac{p\hat{p}}{\sigma^2}\right) \quad (\text{A4})$$

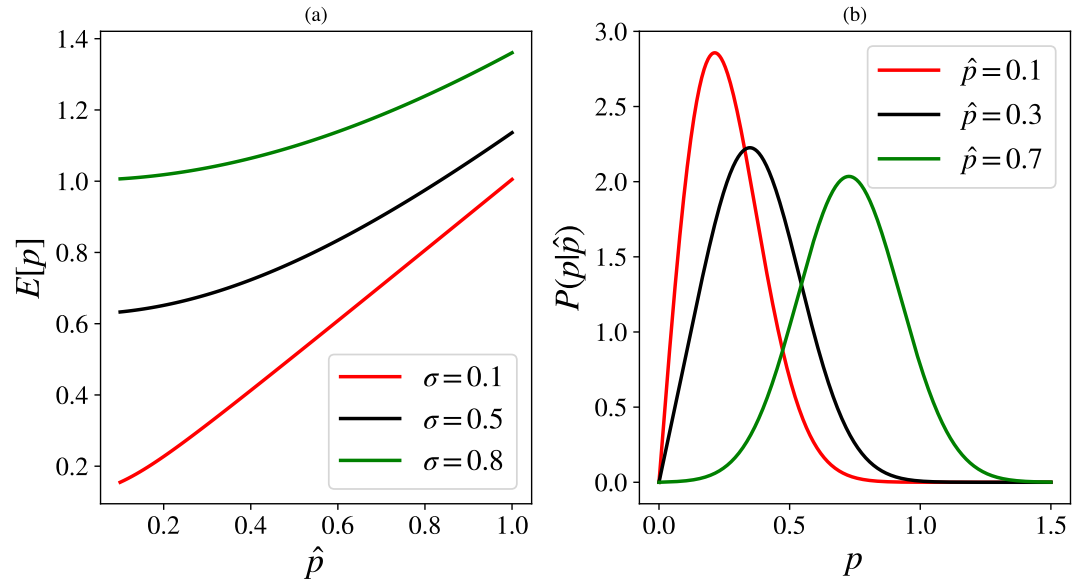


**Figure A1.** (a) Plots of the expected linear polarization fraction measurement,  $E[p]$  as a function of the “true” polarization fraction  $\hat{p}$ , where the expected value is taken as the mean of the corresponding statistical distribution (Equation A6). The plots illustrate the linear polarization bias (i.e. the mismatch between expected and true values) due to  $p$  being an intrinsically positive quantity. The bias exacerbates at larger experimental errors  $\sigma$ . (b) Probability distribution of linear polarization fraction measurements for a variety of “true” values  $\hat{p}$  and  $\sigma = 0.2$ , given in Equation (A5).

where  $I_n(x)$  is the modified Bessel function of the first kind. Rewriting Equation (A4) in terms of the exponentially scaled Bessel function,  $I_0(x) = \exp(|x|)i_0(x)$ , alleviates numerical issues at small  $\sigma$  due to diverging  $I_0(x)$ :

$$P(p|\hat{p}) = \frac{p}{\sigma^2} \exp\left(-\frac{(p-\hat{p})^2}{2\sigma^2}\right) i_0\left(\frac{p\hat{p}}{\sigma^2}\right) \quad (\text{A5})$$

The distribution is plotted in Fig. A1. The value of  $\sigma$  in Equations (A4,A5) may not be known *a priori*. To address this issue, we calculate the expected value,  $E[p]$ , and the variance,  $\text{Var}[p]$ , of  $p$  using the derived distribution:

$$E[p] = \int_0^\infty pP(p|\hat{p})dp = \frac{\sqrt{\pi}}{2\sqrt{2}\sigma} \exp\left(-\frac{\hat{p}^2}{4\sigma^2}\right) \left( (\hat{p}^2 + 2\sigma^2)I_0\left(\frac{\hat{p}^2}{4\sigma^2}\right) + \hat{p}^2 I_1\left(\frac{\hat{p}^2}{4\sigma^2}\right) \right) \quad (\text{A6})$$

$$\text{Var}[p] = E[p^2] - (E[p])^2 = \int_0^\infty p^2P(p|\hat{p})dp - (E[p])^2 = \hat{p}^2 + 2\sigma^2 - (E[p])^2 \quad (\text{A7})$$

Note that, in general,  $E[p] \neq \hat{p}$  due to the polarization degree bias. This effect is demonstrated in Fig. A1. For a given polarization measurement ( $E[p]$  or  $\hat{p}$  depending on whether the value was debiased or not) and its uncertainty ( $\sqrt{\text{Var}[p]}$ ), one may solve Equations (A6,A7) simultaneously for  $\sigma$ .

## References

1. Friedman, A.S.; Gerasimov, R.; Leon, D.; Stevens, W.; Tytler, D.; Keating, B.G.; Kislak, F. Improved constraints on anisotropic birefringent Lorentz invariance and C P T violation from broadband optical polarimetry of high redshift galaxies. *Phys. Rev. D* **2020**, *102*, 043008, [arXiv:astro-ph.HE/2003.00647]. doi:10.1103/PhysRevD.102.043008.
2. Kislak, F.; Krawczynski, H. Planck-scale constraints on anisotropic Lorentz and C P T invariance violations from optical polarization measurements. *Phys. Rev. D* **2017**, *95*, 083013, [arXiv:astro-ph.HE/1701.00437]. doi:10.1103/PhysRevD.95.083013.
3. Kislak, F. Constraints on Lorentz Invariance Violation from Optical Polarimetry of Astrophysical Objects. *Symmetry* **2018**, *10*. doi:10.3390/sym10110596.
4. Tanabashi, M.; Hagiwara, K.; Hikasa, K.; Nakamura, K.; Sumino, Y.; Takahashi, F.; Tanaka, J.; Agashe, K.; Aielli, G.; Amsler, C.; Antonelli, M.; Asner, D.M.; Baer, H.; Banerjee, S.; Barnett, R.M.; Basaglia, T.; Bauer, C.W.; Beatty, J.J.; Belousov, V.I.; Beringer, J.; Bethke, S.; Bettini, A.; Bichsel, H.; Biebel, O.; Black, K.M.; Blucher, E.; Buchmuller, O.; Burkert, V.; Bychkov, M.A.; Cahn, R.N.; Carena, M.; Ceccucci, A.; Cerri, A.; Chakraborty, D.; Chen, M.C.; Chivukula, R.S.; Cowan, G.; Dahl, O.; D'Ambrosio, G.; Damour, T.; de Florian, D.; de Gouvêa, A.; DeGrand, T.; de Jong, P.; Dissertori, G.; Dobrescu, B.A.; D'Onofrio, M.; Doser, M.; Drees, M.; Dreiner, H.K.; Dwyer, D.A.; Eerola, P.; Eidelman, S.; Ellis, J.; Erler, J.; Ezhela, V.V.; Fetscher, W.; Fields, B.D.; Firestone, R.; Foster, B.; Freitas, A.; Gallagher, H.; Garren, L.; Gerber, H.J.; Gerbier, G.; Gershon, T.; Gershtein, Y.; Gherghetta, T.; Godizov, A.A.; Goodman, M.; Grab, C.; Gribsan, A.V.; Grojean, C.; Groom, D.E.; Grünwald, M.; Gurtu, A.; Gutsche, T.; Haber, H.E.; Hanhart, C.; Hashimoto, S.; Hayato, Y.; Hayes, K.G.; Hebecker, A.; Heinemeyer, S.; Heltsley, B.; Hernández-Rey, J.J.; Hisano, J.; Höcker, A.; Holder, J.; Holtkamp, A.; Hyodo, T.; Irwin, K.D.; Johnson, K.F.; Kado, M.; Karliner, M.; Katz, U.F.; Klein, S.R.; Klempt, E.; Kowalewski, R.V.; Krauss, F.; Kreps, M.; Krusche, B.; Kuyanov, Y.V.; Kwon, Y.; Lahav, O.; Laiho, J.; Lesgourgues, J.; Liddle, A.; Ligeti, Z.; Lin, C.J.; Lippmann, C.; Liss, T.M.; Littenberg, L.; Lugovsky, K.S.; Lugovsky, S.B.; Lusiani, A.; Makida, Y.; Maltoni, F.; Mannel, T.; Manohar, A.V.; Marciano, W.J.; Martin, A.D.; Masoni, A.; Matthews, J.; Meißner, U.G.; Milstead, D.; Mitchell, R.E.; Mönig, K.; Molaro, P.; Moortgat, F.; Moskovic, M.; Murayama, H.; Narain, M.; Nason, P.; Navas, S.; Neubert, M.; Nevski, P.; Nir, Y.; Olive, K.A.; Pagan Griso, S.; Parsons, J.; Patrignani, C.; Peacock, J.A.; Pennington, M.; Petcov, S.T.; Petrov, V.A.; Pianori, E.; Piepke, A.; Pomarol, A.; Quadt, A.; Rademacker, J.; Raffelt, G.; Ratcliff, B.N.; Richardson, P.; Ringwald, A.; Roesler, S.; Rolli, S.; Romaniouk, A.; Rosenberg, L.J.; Rosner, J.L.; Rybka, G.; Ryutin, R.A.; Sachrajda, C.T.; Sakai, Y.; Salam, G.P.; Sarkar, S.; Sauli, F.; Schneider, O.; Scholberg, K.; Schwartz, A.J.; Scott, D.; Sharma, V.; Sharpe, S.R.; Shutt, T.; Silari, M.; Sjöstrand, T.; Skands, P.; Skwarnicki, T.; Smith, J.G.; Smoot, G.F.; Spanier, S.; Spieler, H.; Spiering, C.; Stahl, A.; Stone, S.L.; Sumiyoshi, T.; Syphers, M.J.; Terashi, K.; Terning, J.; Thoma, U.; Thorne, R.S.; Tiator, L.; Titov, M.; Tkachenko, N.P.; Törnqvist, N.A.; Tovey, D.R.; Valencia, G.; Van de Water, R.; Varelas, N.; Venanzoni, G.; Verde, L.; Vinciter, M.G.; Vogel, P.; Vogt, A.; Wakely, S.P.; Walkowiak, W.; Walter, C.W.; Wands, D.; Ward, D.R.; Wascko, M.O.; Weiglein, G.; Weinberg, D.H.; Weinberg, E.J.; White, M.; Wiencke, L.R.; Willocq, S.; Wohl, C.G.; Womersley, J.; Woody, C.L.; Workman, R.L.; Yao, W.M.; Zeller, G.P.; Zenin, O.V.; Zhu, R.Y.; Zhu, S.L.;

- Zimmermann, F.; Zyla, P.A.; Anderson, J.; Fuller, L.; Lugovsky, V.S.; Schaffner, P. Review of Particle Physics. *Phys. Rev. D* **2018**, *98*, 030001. doi:10.1103/PhysRevD.98.030001.
5. Aaij, R.; others. Test of lepton universality in beauty-quark decays **2021**. [arXiv:hep-ex/2103.11769].
  6. Myers, R.C.; Pospelov, M. Ultraviolet Modifications of Dispersion Relations in Effective Field Theory. *Phys. Rev. Lett.* **2003**, *90*, 211601, [arXiv:hep-ph/hep-ph/0301124]. doi:10.1103/PhysRevLett.90.211601.
  7. Rizzo, T.G. Lorentz violation in extra dimensions. *Journal of High Energy Physics* **2005**, *2005*, 036, [arXiv:hep-ph/hep-ph/0506056]. doi:10.1088/1126-6708/2005/09/036.
  8. Amelino-Camelia, G.; Guetta, D.; Piran, T. ICECUBE Neutrinos and Lorentz Invariance Violation. *ApJ* **2015**, *806*, 269. doi:10.1088/0004-637X/806/2/269.
  9. Kostelecký, V.A.; Samuel, S. Spontaneous breaking of Lorentz symmetry in string theory. *Phys. Rev. D* **1989**, *39*, 683–685. doi:10.1103/PhysRevD.39.683.
  10. Burgess, C.P.; Cline, J.M.; Filotas, E.; Matias, J.; Moore, G.D. Loop-generated bounds on changes to the graviton dispersion relation. *Journal of High Energy Physics* **2002**, *2002*, 043, [arXiv:hep-ph/hep-ph/0201082]. doi:10.1088/1126-6708/2002/03/043.
  11. Gambini, R.; Pullin, J. Nonstandard optics from quantum space-time. *Phys. Rev. D* **1999**, *59*, 124021, [arXiv:gr-qc/gr-qc/9809038]. doi:10.1103/PhysRevD.59.124021.
  12. Pospelov, M.; Shang, Y. Lorentz violation in Hořava-Lifshitz-type theories. *Phys. Rev. D* **2012**, *85*, 105001, [arXiv:hep-th/1010.5249]. doi:10.1103/PhysRevD.85.105001.
  13. Li, M.; Cai, Y.F.; Wang, X.; Zhang, X. CPT violating electrodynamics and Chern-Simons modified gravity. *Physics Letters B* **2009**, *680*, 118–124, [arXiv:hep-ph/0907.5159]. doi:10.1016/j.physletb.2009.08.053.
  14. Kostelecký, V.A.; Potting, R. CPT, strings, and meson factories. *Phys. Rev. D* **1995**, *51*, 3923–3935, [arXiv:hep-ph/hep-ph/9501341]. doi:10.1103/PhysRevD.51.3923.
  15. Kostelecký, V.A.; Mewes, M. Electrodynamics with Lorentz-violating operators of arbitrary dimension. *Phys. Rev. D* **2009**, *80*, 015020, [arXiv:hep-ph/0905.0031]. doi:10.1103/PhysRevD.80.015020.
  16. Adamson, P.; others. A Search for Lorentz Invariance and CPT Violation with the MINOS Far Detector. *Phys. Rev. Lett.* **2010**, *105*, 151601, [arXiv:hep-ex/1007.2791]. doi:10.1103/PhysRevLett.105.151601.
  17. Adamson, P.; others. Search for Lorentz invariance and CPT violation with muon antineutrinos in the MINOS Near Detector. *Phys. Rev. D* **2012**, *85*, 031101, [arXiv:hep-ex/1201.2631]. doi:10.1103/PhysRevD.85.031101.
  18. Mattingly, D. Modern Tests of Lorentz Invariance. *Living Reviews in Relativity* **2005**, *8*, 5, [arXiv:gr-qc/gr-qc/0502097]. doi:10.12942/lrr-2005-5.
  19. Aaij, R.; others. Search for violations of Lorentz invariance and CPT symmetry in  $B_{(s)}^0$  mixing. *Phys. Rev. Lett.* **2016**, *116*, 241601, [arXiv:hep-ex/1603.04804]. doi:10.1103/PhysRevLett.116.241601.
  20. Carle, A.; Chanon, N.; Perries, S. Prospects for Lorentz Invariance Violation searches with top pair production at the LHC and future hadron colliders. *Eur. Phys. J. C* **2020**, *80*, 128, [arXiv:hep-ph/1908.11256]. doi:10.1140/epjc/s10052-020-7715-2.
  21. Colladay, D.; Kostelecký, V.A. CPT violation and the standard model. *Phys. Rev. D* **1997**, *55*, 6760–6774, [arXiv:hep-ph/hep-ph/9703464]. doi:10.1103/PhysRevD.55.6760.
  22. Colladay, D.; Kostelecký, V.A. Lorentz-violating extension of the standard model. *Phys. Rev. D* **1998**, *58*, 116002, [arXiv:astro-ph/hep-ph/9809521]. doi:10.1103/PhysRevD.58.116002.
  23. Kostelecký, V.A.; Mewes, M. Signals for Lorentz violation in electrodynamics. *Phys. Rev. D* **2002**, *66*, 056005, [arXiv:hep-ph/hep-ph/0205211]. doi:10.1103/PhysRevD.66.056005.
  24. Kostelecký, V.A. Gravity, Lorentz violation, and the standard model. *Phys. Rev. D* **2004**, *69*, 105009, [arXiv:hep-th/hep-th/0312310]. doi:10.1103/PhysRevD.69.105009.
  25. Kislak, F.; Krawczynski, H. Search for anisotropic Lorentz invariance violation with  $\gamma$  -rays. *Phys. Rev. D* **2015**, *92*, 045016, [arXiv:astro-ph.HE/1505.02669]. doi:10.1103/PhysRevD.92.045016.
  26. Vasileiou, V.; Jacholkowska, A.; Piron, F.; Bolmont, J.; Couturier, C.; Granot, J.; Stecker, F.W.; Cohen-Tanugi, J.; Longo, F. Constraints on Lorentz invariance violation from Fermi-Large Area Telescope observations of gamma-ray bursts. *Phys. Rev. D* **2013**, *87*, 122001, [arXiv:astro-ph.HE/1305.3463]. doi:10.1103/PhysRevD.87.122001.
  27. Boggs, S.E.; Wunderer, C.B.; Hurley, K.; Coburn, W. Testing Lorentz Invariance with GRB 021206. *ApJ* **2004**, *611*, L77–L80, [arXiv:astro-ph/astro-ph/0310307]. doi:10.1086/423933.
  28. Aharonian, F.; Akhperjanian, A.G.; Barres de Almeida, U.; Bazer-Bachi, A.R.; Becherini, Y.; Behera, B.; Beilicke, M.; Benbow, W.; Bernlöhr, K.; Boisson, C.; Bochow, A.; Borrel, V.; Brion, I.; Brucker, J.; Brun, P.; Bühler, R.; Bulik, T.; Büsching, I.; Boutelier, T.; Carrigan, S.; Chadwick, P.M.; Charbonnier, A.; Chaves, R.C.G.; Chounet, L.M.; Clapson, A.C.; Coignet, G.; Costamante, L.; Dalton, M.; Degrange, B.; Deil, C.; Dickinson, H.J.; Djannati-Ataï, A.; Domainko, W.; Drury, L.O.C.; Dubois, F.; Dubus, G.; Dyks, J.; Egberts, K.; Emmanoulopoulos, D.; Espigat, P.; Farnier, C.; Feinstein, F.; Fiasson, A.; Förster, A.; Fontaine, G.; Füßling, M.; Gabici, S.; Gallant, Y.A.; Gérard, L.; Giebels, B.; Glicenstein, J.F.; Glück, B.; Goret, P.; Hadjichristidis, C.; Hauser, D.; Hauser, M.; Heinz, S.; Heinzlmann, G.; Henri, G.; Hermann, G.; Hinton, J.A.; Hoffmann, A.; Hofmann, W.; Holleran, M.; Hoppe, S.; Horns, D.; Jacholkowska, A.; de

- Jager, O.C.; Jung, I.; Katarzyński, K.; Kaufmann, S.; Kendziorra, E.; Kerschhaggl, M.; Khangulyan, D.; Khélifi, B.; Keogh, D.; Komin, N.; Kosack, K.; Lamanna, G.; Lenain, J.P.; Lohse, T.; Marandon, V.; Martin, J.M.; Martineau-Huynh, O.; Marcowith, A.; Maurin, D.; McComb, T.J.L.; Medina, C.; Moderski, R.; Moulin, E.; Naumann-Godo, M.; de Naurois, M.; Nedbal, D.; Nekrassov, D.; Niemiec, J.; Nolan, S.J.; Ohm, S.; Olive, J.F.; de Oña Wilhelmi, E.; Orford, K.J.; Osborne, J.L.; Ostrowski, M.; Panter, M.; Pedalletti, G.; Pelletier, G.; Petrucci, P.O.; Pita, S.; Pühlhofer, G.; Punch, M.; Quirrenbach, A.; Raubenheimer, B.C.; Raue, M.; Rayner, S.M.; Renaud, M.; Rieger, F.; Ripken, J.; Rob, L.; Rosier-Lees, S.; Rowell, G.; Rudak, B.; Ruppel, J.; Sahakian, V.; Santangelo, A.; Schlickeiser, R.; Schöck, F.M.; Schröder, R.; Schwanke, U.; Schwarzburg, S.; Schwemmer, S.; Shalchi, A.; Skilton, J.L.; Sol, H.; Spangler, D.; Stawarz, Ł.; Steenkamp, R.; Stegmann, C.; Superina, G.; Tam, P.H.; Tavernet, J.P.; Terrier, R.; Tibolla, O.; van Eldik, C.; Vasileiadis, G.; Venter, C.; Vialle, J.P.; Vincent, P.; Vivier, M.; Völk, H.J.; Volpe, F.; Wagner, S.J.; Ward, M.; Zdziarski, A.A.; Zech, A.; H. E. S. S. Collaboration. Limits on an Energy Dependence of the Speed of Light from a Flare of the Active Galaxy PKS 2155-304. *Phys. Rev. Lett.* **2008**, *101*, 170402, [[arXiv:astro-ph/0810.3475](https://arxiv.org/abs/astro-ph/0810.3475)]. doi:10.1103/PhysRevLett.101.170402.
29. Abramowski, A.; Aharonian, F.; Ait Benkhali, F.; Akhperjanian, A.G.; Angüner, E.O.; Backes, M.; Balenderan, S.; Balzer, A.; Barnacka, A.; Becherini, Y.; Becker Tjus, J.; Berge, D.; Bernhard, S.; Bernlöhr, K.; Birsin, E.; Biteau, J.; Böttcher, M.; Boisson, C.; Bolmont, J.; Bordas, P.; Bregeon, J.; Brun, F.; Brun, P.; Bryan, M.; Bulik, T.; Carrigan, S.; Casanova, S.; Chadwick, P.M.; Chakraborty, N.; Chalme-Calvet, R.; Chaves, R.C.G.; Chrétien, M.; Colafrancesco, S.; Cologna, G.; Conrad, J.; Couturier, C.; Cui, Y.; Dalton, M.; Davids, I.D.; Degrange, B.; Deil, C.; deWilt, P.; Djannati-Ataï, A.; Domainko, W.; Donath, A.; O’C. Drury, L.; Dubus, G.; Dutton, K.; Dyks, J.; Dyrda, M.; Edwards, T.; Egberts, K.; Eger, P.; Espigat, P.; Farnier, C.; Fegan, S.; Feinstein, F.; Fernandes, M.V.; Fernandez, D.; Fiaßon, A.; Fontaine, G.; Förster, A.; Füssling, M.; Gabici, S.; Gajdus, M.; Gallant, Y.A.; Garrigoux, T.; Giavitto, G.; Giebels, B.; Glicenstein, J.F.; Gottschall, D.; Grondin, M.H.; Grudzińska, M.; Hadsch, D.; Häffner, S.; Hahn, J.; Harris, J.; Heinzlmann, G.; Henri, G.; Hermann, G.; Hervet, O.; Hillert, A.; Hinton, J.A.; Hofmann, W.; Hofverberg, P.; Holler, M.; Horns, D.; Ivascenko, A.; Jacholkowska, A.; Jahn, C.; Jamrozy, M.; Janiak, M.; Jankowsky, F.; Jung, I.; Kastendieck, M.A.; Katarzyński, K.; Katz, U.; Kaufmann, S.; Khélifi, B.; Kieffer, M.; Klepser, S.; Klochkov, D.; Kluzniak, W.; Kolitzus, D.; Komin, N.; Kosack, K.; Krakau, S.; Krayzel, F.; Krüger, P.P.; Laffon, H.; Lamanna, G.; Lefaucheur, J.; Lefranc, V.; Lemiére, A.; Lemoine-Goumard, M.; Lenain, J.P.; Lohse, T.; Lopatin, A.; Lu, C.C.; Marandon, V.; Marcowith, A.; Marx, R.; Maurin, G.; Maxted, N.; Mayer, M.; McComb, T.J.L.; Méhault, J.; Meintjes, P.J.; Menzler, U.; Meyer, M.; Mitchell, A.M.W.; Moderski, R.; Mohamed, M.; Morå, K.; Moulin, E.; Murach, T.; de Naurois, M.; Niemiec, J.; Nolan, S.J.; Oakes, L.; Odaka, H.; Ohm, S.; Opitz, B.; Ostrowski, M.; Oya, I.; Panter, M.; Parsons, R.D.; Paz Arribas, M.; Pekeur, N.W.; Pelletier, G.; Perez, J.; Petrucci, P.O.; Peyaud, B.; Pita, S.; Poon, H.; Pühlhofer, G.; Punch, M.; Quirrenbach, A.; Raab, S.; Reichardt, I.; Reimer, A.; Reimer, O.; Renaud, M.; de los Reyes, R.; Rieger, F.; Rob, L.; Romoli, C.; Rosier-Lees, S.; Rowell, G.; Rudak, B.; Rulten, C.B.; Sahakian, V.; Salek, D.; Sanchez, D.A.; Santangelo, A.; Schlickeiser, R.; Schüssler, F.; Schulz, A.; Schwanke, U.; Schwarzburg, S.; Schwemmer, S.; Sol, H.; Spanier, F.; Spengler, G.; Spies, F.; Stawarz, Ł.; Steenkamp, R.; Stegmann, C.; Stinzing, F.; Stycz, K.; Sushch, I.; Tavernet, J.P.; Tavernier, T.; Taylor, A.M.; Terrier, R.; Tluczykont, M.; Trichard, C.; Valerius, K.; van Eldik, C.; van Soelen, B.; Vasileiadis, G.; Veh, J.; Venter, C.; Viana, A.; Vincent, P.; Vink, J.; Völk, H.J.; Volpe, F.; Vorster, M.; Vuillaume, T.; Wagner, P.; Wagner, R.M.; Ward, M.; Weidinger, M.; Weitzel, Q.; White, R.; Wiercholska, A.; Willmann, P.; Wörnlein, A.; Wouters, D.; Yang, R.; Zabalza, V.; Zaborov, D.; Zacharias, M.; Zdziarski, A.A.; Zech, A.; Zechlin, H.S.; H. E. S. S. Collaboration. The 2012 Flare of PG 1553+113 Seen with H.E.S.S. and Fermi-LAT. *ApJ* **2015**, *802*, 65, [[arXiv:astro-ph.HE/1501.05087](https://arxiv.org/abs/astro-ph.HE/1501.05087)]. doi:10.1088/0004-637X/802/1/65.
30. Albert, J.; others. Probing Quantum Gravity using Photons from a flare of the active galactic nucleus Markarian 501 Observed by the MAGIC telescope. *Phys. Lett. B* **2008**, *668*, 253–257, [[arXiv:astro-ph/0708.2889](https://arxiv.org/abs/astro-ph/0708.2889)]. doi:10.1016/j.physletb.2008.08.053.
31. Biller, S.D.; Breslin, A.C.; Buckley, J.; Catanese, M.; Carson, M.; Carter-Lewis, D.A.; Cawley, M.F.; Fegan, D.J.; Finley, J.P.; Gaidos, J.A.; Hillas, A.M.; Krennrich, F.; Lamb, R.C.; Lessard, R.; Masterson, C.; McEnery, J.E.; McKernan, B.; Moriarty, P.; Quinn, J.; Rose, H.J.; Samuelson, F.; Sembroski, G.; Skelton, P.; Weekes, T.C. Limits to Quantum Gravity Effects on Energy Dependence of the Speed of Light from Observations of TeV Flares in Active Galaxies. *Phys. Rev. Lett.* **1999**, *83*, 2108–2111, [[arXiv:gr-qc/9810044](https://arxiv.org/abs/gr-qc/9810044)]. doi:10.1103/PhysRevLett.83.2108.
32. Ellis, J.; Mavromatos, N.E.; Nanopoulos, D.V.; Sakharov, A.S.; Sarkisyan, E.K.G. Robust limits on Lorentz violation from gamma-ray bursts. *Astroparticle Physics* **2006**, *25*, 402–411, [[arXiv:astro-ph/astro-ph/0510172](https://arxiv.org/abs/astro-ph/astro-ph/0510172)]. doi:10.1016/j.astropartphys.2006.04.001.
33. Wei, J.J.; Wu, X.F. A Further Test of Lorentz Violation from the Rest-frame Spectral Lags of Gamma-Ray Bursts. *ApJ* **2017**, *851*, 127, [[arXiv:astro-ph/1711.09185](https://arxiv.org/abs/astro-ph/1711.09185)]. doi:10.3847/1538-4357/aa9d8d.
34. Wei, J.J.; Wu, X.F. Testing fundamental physics with astrophysical transients. *Frontiers of Physics* **2021**, *16*, 44300, [[arXiv:astro-ph.HE/2102.03724](https://arxiv.org/abs/astro-ph.HE/2102.03724)]. doi:10.1007/s11467-021-1049-x.
35. Kaaret, P. X-ray clues to viability of loop quantum gravity. *Nature* **2004**, *427*, 287. doi:10.1038/427287b.
36. Kostelecký, V.A.; Mewes, M. Constraints on Relativity Violations from Gamma-Ray Bursts. *Phys. Rev. Lett.* **2013**, *110*, 201601, [[arXiv:astro-ph.HE/1301.5367](https://arxiv.org/abs/astro-ph.HE/1301.5367)]. doi:10.1103/PhysRevLett.110.201601.
37. Toma, K.; Mukohyama, S.; Yonetoku, D.; Murakami, T.; Gunji, S.; Mihara, T.; Morihara, Y.; Sakashita, T.; Takahashi, T.; Wakashima, Y.; Yonemochi, H.; Toukairin, N. Strict Limit on CPT Violation from Polarization of  $\gamma$ -Ray Bursts. *Phys. Rev. Lett.* **2012**, *109*, 241104, [[arXiv:astro-ph.HE/1208.5288](https://arxiv.org/abs/astro-ph.HE/1208.5288)]. doi:10.1103/PhysRevLett.109.241104.

38. Laurent, P.; Götz, D.; Binétruy, P.; Covino, S.; Fernandez-Soto, A. Constraints on Lorentz Invariance Violation using integral/IBIS observations of GRB041219A. *Phys. Rev. D* **2011**, *83*, 121301, [arXiv:astro-ph.HE/1106.1068]. doi:10.1103/PhysRevD.83.121301.
39. Stecker, F.W. A new limit on Planck scale Lorentz violation from  $\gamma$ -ray burst polarization. *Astroparticle Physics* **2011**, *35*, 95–97, [arXiv:astro-ph.HE/1102.2784]. doi:10.1016/j.astropartphys.2011.06.007.
40. Kostelecký, V.A.; Russell, N. Data tables for Lorentz and CPT violation. *Reviews of Modern Physics* **2011**, *83*, 11–32, [arXiv:hep-ph/0801.0287]. doi:10.1103/RevModPhys.83.11.
41. Kostelecký, V.A.; Mewes, M. Astrophysical Tests of Lorentz and CPT Violation with Photons. *ApJ* **2008**, *689*, L1, [arXiv:astro-ph/0809.2846]. doi:10.1086/595815.
42. Jacob, U.; Piran, T. Lorentz-violation-induced arrival delays of cosmological particles. *J. Cosmology Astropart. Phys.* **2008**, *2008*, 031, [arXiv:astro-ph/0712.2170]. doi:10.1088/1475-7516/2008/01/031.
43. Contopoulos, G.; Jappel, A. *Transactions of the International Astronomical Union, Volume\_XVB: Proceedings of the Fifteenth General Assembly, Sydney 1973 and Extraordinary Assembly, Poland 1973.*; 1974.
44. Fomalont, E. The International Celestial Reference System. The Science of Calibration; Deustua, S.; Allam, S.; Tucker, D.; Smith, J.A., Eds., 2016, Vol. 503, *Astronomical Society of the Pacific Conference Series*, p. 177.
45. McKinnon, M.M. Three-Dimensional Statistics of Radio Polarimetry. *ApJS* **2003**, *148*, 519–526, [arXiv:astro-ph/astro-ph/0306063]. doi:10.1086/376898.
46. Planck Collaboration.; Aghanim, N.; Akrami, Y.; Ashdown, M.; Aumont, J.; Baccigalupi, C.; Ballardini, M.; Banday, A.J.; Barreiro, R.B.; Bartolo, N.; Basak, S.; Battye, R.; Benabed, K.; Bernard, J.P.; Bersanelli, M.; Bielewicz, P.; Bock, J.J.; Bond, J.R.; Borrill, J.; Bouchet, F.R.; Boulanger, F.; Bucher, M.; Burigana, C.; Butler, R.C.; Calabrese, E.; Cardoso, J.F.; Carron, J.; Challinor, A.; Chiang, H.C.; Chluba, J.; Colombo, L.P.L.; Combet, C.; Contreras, D.; Crill, B.P.; Cuttaia, F.; de Bernardis, P.; de Zotti, G.; Delabrouille, J.; Delouis, J.M.; Di Valentino, E.; Diego, J.M.; Doré, O.; Douspis, M.; Ducout, A.; Dupac, X.; Dusini, S.; Efstathiou, G.; Elsner, F.; Enßlin, T.A.; Eriksen, H.K.; Fantaye, Y.; Farhang, M.; Fergusson, J.; Fernandez-Cobos, R.; Finelli, F.; Forastieri, F.; Frailis, M.; Fraisse, A.A.; Franceschi, E.; Frolov, A.; Galeotta, S.; Galli, S.; Ganga, K.; Génova-Santos, R.T.; Gerbino, M.; Ghosh, T.; González-Nuevo, J.; Górski, K.M.; Gratton, S.; Gruppuso, A.; Gudmundsson, J.E.; Hamann, J.; Handley, W.; Hansen, F.K.; Herranz, D.; Hildebrandt, S.R.; Hivon, E.; Huang, Z.; Jaffe, A.H.; Jones, W.C.; Karakci, A.; Keihänen, E.; Keskitalo, R.; Kiiveri, K.; Kim, J.; Kisner, T.S.; Knox, L.; Krachmalnicoff, N.; Kunz, M.; Kurki-Suonio, H.; Lagache, G.; Lamarre, J.M.; Lasenby, A.; Lattanzi, M.; Lawrence, C.R.; Le Jeune, M.; Lemos, P.; Lesgourgues, J.; Levrier, F.; Lewis, A.; Liguori, M.; Lilje, P.B.; Lilley, M.; Lindholm, V.; López-Cañiego, M.; Lubin, P.M.; Ma, Y.Z.; Macías-Pérez, J.F.; Maggio, G.; Maino, D.; Mandolesi, N.; Mangilli, A.; Marcos-Caballero, A.; Maris, M.; Martin, P.G.; Martinelli, M.; Martínez-González, E.; Matarrese, S.; Mauri, N.; McEwen, J.D.; Meinhold, P.R.; Melchiorri, A.; Mennella, A.; Migliaccio, M.; Millea, M.; Mitra, S.; Miville-Deschênes, M.A.; Molinari, D.; Montier, L.; Morgante, G.; Moss, A.; Natoli, P.; Nørgaard-Nielsen, H.U.; Pagano, L.; Paoletti, D.; Partridge, B.; Patanchon, G.; Peiris, H.V.; Perrotta, F.; Pettorino, V.; Piacentini, F.; Polastri, L.; Polenta, G.; Puget, J.L.; Rachen, J.P.; Reinecke, M.; Remazeilles, M.; Renzi, A.; Rocha, G.; Rosset, C.; Roudier, G.; Rubiño-Martín, J.A.; Ruiz-Granados, B.; Salvati, L.; Sandri, M.; Savelainen, M.; Scott, D.; Shellard, E.P.S.; Sirignano, C.; Sirri, G.; Spencer, L.D.; Sunyaev, R.; Suur-Uski, A.S.; Tauber, J.A.; Tavagnacco, D.; Tenti, M.; Toffolatti, L.; Tomasi, M.; Trombetti, T.; Valenziano, L.; Valiviita, J.; Van Tent, B.; Vibert, L.; Vielva, P.; Villa, F.; Vittorio, N.; Wandelt, B.D.; Wehus, I.K.; White, M.; White, S.D.M.; Zacchei, A.; Zonca, A. Planck 2018 results. VI. Cosmological parameters. *A&A* **2020**, *641*, A6, [arXiv:astro-ph.CO/1807.06209]. doi:10.1051/0004-6361/201833910.
47. Shao, L. Combined search for anisotropic birefringence in the gravitational-wave transient catalog GWTC-1. *Phys. Rev. D* **2020**, *101*, 104019, [arXiv:hep-ph/2002.01185]. doi:10.1103/PhysRevD.101.104019.
48. Komatsu, E.; Dunkley, J.; Nolta, M.R.; Bennett, C.L.; Gold, B.; Hinshaw, G.; Jarosik, N.; Larson, D.; Limon, M.; Page, L.; Spergel, D.N.; Halpern, M.; Hill, R.S.; Kogut, A.; Meyer, S.S.; Tucker, G.S.; Weiland, J.L.; Wollack, E.; Wright, E.L. Five-Year Wilkinson Microwave Anisotropy Probe Observations: Cosmological Interpretation. *ApJS* **2009**, *180*, 330–376, [arXiv:astro-ph/0803.0547]. doi:10.1088/0067-0049/180/2/330.
49. Gubitosi, G.; Pagano, L.; Amelino-Camelia, G.; Melchiorri, A.; Cooray, A. A constraint on Planck-scale modifications to electrodynamics with CMB polarization data. *J. Cosmology Astropart. Phys.* **2009**, *2009*, 021, [arXiv:astro-ph.CO/0904.3201]. doi:10.1088/1475-7516/2009/08/021.
50. Kahnashvili, T.; Durrer, R.; Maravin, Y. Testing Lorentz invariance violation with Wilkinson Microwave Anisotropy Probe five year data. *Phys. Rev. D* **2008**, *78*, 123009, [arXiv:astro-ph/0807.2593]. doi:10.1103/PhysRevD.78.123009.
51. Kaufman, J.P.; Keating, B.G.; Johnson, B.R. Precision tests of parity violation over cosmological distances. *MNRAS* **2016**, *455*, 1981–1988, [arXiv:astro-ph.CO/1409.8242]. doi:10.1093/mnras/stv2348.
52. Leon, D.; Kaufman, J.; Keating, B.; Mewes, M. The cosmic microwave background and pseudo-Nambu-Goldstone bosons: Searching for Lorentz violations in the cosmos. *Modern Physics Letters A* **2017**, *32*, 1730002, [arXiv:astro-ph.CO/1611.00418]. doi:10.1142/S0217732317300026.
53. Buzzoni, B.; Delabre, B.; Dekker, H.; Dodorico, S.; Enard, D.; Focardi, P.; Gustafsson, B.; Nees, W.; Paureau, J.; Reiss, R. The ESO Faint Object Spectrograph and Camera / EFOSC. *The Messenger* **1984**, *38*, 9.

- 
54. Hutsemékers, D.; Borguet, B.; Sluse, D.; Cabanac, R.; Lamy, H. Optical circular polarization in quasars. *A&A* **2010**, *520*, L7, [[arXiv:astro-ph.CO/1009.4049](#)]. doi:10.1051/0004-6361/201015359.
  55. Matsumiya, M.; Ioka, K. Circular Polarization from Gamma-Ray Burst Afterglows. *ApJ* **2003**, *595*, L25–L28, [[arXiv:astro-ph/astro-ph/0307462](#)]. doi:10.1086/378879.
  56. Sagiv, A.; Waxman, E.; Loeb, A. Probing the Magnetic Field Structure in Gamma-Ray Bursts through Dispersive Plasma Effects on the Afterglow Polarization. *ApJ* **2004**, *615*, 366–377, [[arXiv:astro-ph/astro-ph/0401620](#)]. doi:10.1086/423977.
  57. Toma, K.; Ioka, K.; Nakamura, T. Probing the Efficiency of Electron-Proton Coupling in Relativistic Collisionless Shocks through the Radio Polarimetry of Gamma-Ray Burst Afterglows. *ApJ* **2008**, *673*, L123, [[arXiv:astro-ph/0709.3332](#)]. doi:10.1086/528740.
  58. Hutsemékers, D.; Borguet, B.; Sluse, D.; Cabanac, R.; Lamy, H. Optical circular polarization in quasars. *A&A* **2010**, *520*, L7, [[arXiv:astro-ph.CO/1009.4049](#)]. doi:10.1051/0004-6361/201015359.
  59. Impey, C.D.; Tapia, S. The Optical Polarization Properties of Quasars. *ApJ* **1990**, *354*, 124. doi:10.1086/168672.
  60. Berriman, G.; Schmidt, G.D.; West, S.C.; Stockman, H.S. An Optical Polarization Survey of the Palomar-Green Bright Quasar Sample. *ApJS* **1990**, *74*, 869. doi:10.1086/191523.
  61. Hutsemékers, D.; Lamy, H.; Remy, M. Polarization properties of a sample of broad absorption line and gravitationally lensed quasars. *A&A* **1998**, *340*, 371–380.
  62. Visvanathan, N.; Wills, B.J. Optical Polarization of 52 Radio-loud QSOS and BL Lacertae Objects. *AJ* **1998**, *116*, 2119–2122, [[arXiv:astro-ph/astro-ph/9808060](#)]. doi:10.1086/300610.
  63. Schmidt, G.D.; Hines, D.C. The Polarization of Broad Absorption Line QSOS. *ApJ* **1999**, *512*, 125–135. doi:10.1086/306770.
  64. Lamy, H.; Hutsemékers, D. Optical polarization of 47 quasi-stellar objects: The data. *A&AS* **2000**, *142*, 451–456. doi:10.1051/aas:2000165.
  65. Sluse, D.; Hutsemékers, D.; Lamy, H.; Cabanac, R.; Quintana, H. New optical polarization measurements of quasi-stellar objects. The data. *A&A* **2005**, *433*, 757–764, [[arXiv:astro-ph/astro-ph/0507023](#)]. doi:10.1051/0004-6361:20042163.
  66. Breger, M. Intracuster dust, circumstellar shells, and the wavelength dependence of polarization in Orion. *ApJ* **1977**, *215*, 119–128. doi:10.1086/155339.
  67. Visvanathan, N. An Automatic Fast Digital-Photoelectric Photometer with Polarimeter. *PASP* **1972**, *84*, 248. doi:10.1086/129279.
  68. Abazajian, K.N.; Adelman-McCarthy, J.K.; Agüeros, M.A.; Allam, S.S.; Allende Prieto, C.; An, D.; Anderson, K.S.J.; Anderson, S.F.; Annis, J.; Bahcall, N.A.; Bailer-Jones, C.A.L.; Barentine, J.C.; Bassett, B.A.; Becker, A.C.; Beers, T.C.; Bell, E.F.; Belokurov, V.; Berlind, A.A.; Berman, E.F.; Bernardi, M.; Bickerton, S.J.; Bizyaev, D.; Blakeslee, J.P.; Blanton, M.R.; Bochanski, J.J.; Boroski, W.N.; Brewington, H.J.; Brinchmann, J.; Brinkmann, J.; Brunner, R.J.; Budavári, T.; Carey, L.N.; Carliles, S.; Carr, M.A.; Castander, F.J.; Cinabro, D.; Connolly, A.J.; Csabai, I.; Cunha, C.E.; Czarapata, P.C.; Davenport, J.R.A.; de Haas, E.; Dilday, B.; Doi, M.; Eisenstein, D.J.; Evans, M.L.; Evans, N.W.; Fan, X.; Friedman, S.D.; Frieman, J.A.; Fukugita, M.; Gänsicke, B.T.; Gates, E.; Gillespie, B.; Gilmore, G.; Gonzalez, B.; Gonzalez, C.F.; Grebel, E.K.; Gunn, J.E.; Györy, Z.; Hall, P.B.; Harding, P.; Harris, F.H.; Harvanek, M.; Hawley, S.L.; Hayes, J.J.E.; Heckman, T.M.; Hendry, J.S.; Hennessy, G.S.; Hindsley, R.B.; Hoblitt, J.; Hogan, C.J.; Hogg, D.W.; Holtzman, J.A.; Hyde, J.B.; Ichikawa, S.i.; Ichikawa, T.; Im, M.; Ivezić, Ž.; Jester, S.; Jiang, L.; Johnson, J.A.; Jorgensen, A.M.; Jurić, M.; Kent, S.M.; Kessler, R.; Kleinman, S.J.; Knapp, G.R.; Konishi, K.; Kron, R.G.; Krzesinski, J.; Kuropatkin, N.; Lampeitl, H.; Lebedeva, S.; Lee, M.G.; Lee, Y.S.; French Leger, R.; Lépine, S.; Li, N.; Lima, M.; Lin, H.; Long, D.C.; Loomis, C.P.; Loveday, J.; Lupton, R.H.; Magnier, E.; Malanushenko, O.; Malanushenko, V.; Mandelbaum, R.; Margon, B.; Marriner, J.P.; Martínez-Delgado, D.; Matsubara, T.; McGehee, P.M.; McKay, T.A.; Meiksin, A.; Morrison, H.L.; Mullally, F.; Munn, J.A.; Murphy, T.; Nash, T.; Nebot, A.; Neilsen, Eric H., J.; Newberg, H.J.; Newman, P.R.; Nichol, R.C.; Nicinski, T.; Nieto-Santisteban, M.; Nitta, A.; Okamura, S.; Oravetz, D.J.; Ostriker, J.P.; Owen, R.; Padmanabhan, N.; Pan, K.; Park, C.; Pauls, G.; Peoples, John, J.; Percival, W.J.; Pier, J.R.; Pope, A.C.; Pourbaix, D.; Price, P.A.; Purger, N.; Quinn, T.; Raddick, M.J.; Re Fiorentin, P.; Richards, G.T.; Richmond, M.W.; Riess, A.G.; Rix, H.W.; Rockosi, C.M.; Sako, M.; Schlegel, D.J.; Schneider, D.P.; Scholz, R.D.; Schreiber, M.R.; Schwobe, A.D.; Seljak, U.; Sesar, B.; Sheldon, E.; Shimasaku, K.; Sibley, V.C.; Simmons, A.E.; Sivarani, T.; Allyn Smith, J.; Smith, M.C.; Smolčić, V.; Snedden, S.A.; Stebbins, A.; Steinmetz, M.; Stoughton, C.; Strauss, M.A.; SubbaRao, M.; Suto, Y.; Szalay, A.S.; Szapudi, I.; Szkody, P.; Tanaka, M.; Tegmark, M.; Teodoro, L.F.A.; Thakar, A.R.; Tremonti, C.A.; Tucker, D.L.; Uomoto, A.; Vanden Berk, D.E.; Vandenberg, J.; Vidrih, S.; Vogeley, M.S.; Voges, W.; Vogt, N.P.; Wadadekar, Y.; Watters, S.; Weinberg, D.H.; West, A.A.; White, S.D.M.; Wilhite, B.C.; Wonders, A.C.; Yanny, B.; Yocum, D.R.; York, D.G.; Zehavi, I.; Zibetti, S.; Zucker, D.B. The Seventh Data Release of the Sloan Digital Sky Survey. *ApJS* **2009**, *182*, 543–558, [[arXiv:astro-ph/0812.0649](#)]. doi:10.1088/0067-0049/182/2/543.
  69. Truebenbach, A.E.; Darling, J. The VLBA Extragalactic Proper Motion Catalog and a Measurement of the Secular Aberration Drift. *ApJS* **2017**, *233*, 3. doi:10.3847/1538-4365/aa9026.
  70. Jones, D.H.; Read, M.A.; Saunders, W.; Colless, M.; Jarrett, T.; Parker, Q.A.; Fairall, A.P.; Mauch, T.; Sadler, E.M.; Watson, F.G.; Burton, D.; Campbell, L.A.; Cass, P.; Croom, S.M.; Dawe, J.; Fiegert, K.; Frankcombe, L.; Hartley, M.; Huchra, J.; James, D.; Kirby, E.; Lahav, O.; Lucey, J.; Mamon, G.A.; Moore, L.; Peterson, B.A.; Prior, S.; Proust, D.; Russell, K.; Safouris, V.; Wakamatsu, K.I.; Westra, E.; Williams, M. The 6dF Galaxy Survey: final redshift release (DR3) and southern large-scale structures. *MNRAS* **2009**, *399*, 683–698, [[arXiv:astro-ph.CO/0903.5451](#)]. doi:10.1111/j.1365-2966.2009.15338.x.



71. O'Meara, J.M.; Lehner, N.; Howk, J.C.; Prochaska, J.X.; Fox, A.J.; Peeples, M.S.; Tumlinson, J.; O'Shea, B.W. The Second Data Release of the KODIAQ Survey. *AJ* **2017**, *154*, 114, [[arXiv:astro-ph.GA/1707.07905](https://arxiv.org/abs/1707.07905)]. doi:10.3847/1538-3881/aa82b8.
72. Ahn, C.P.; Alexandroff, R.; Allende Prieto, C.; Anderson, S.F.; Anderton, T.; Andrews, B.H.; Aubourg, É.; Bailey, S.; Balbinot, E.; Barnes, R.; Bautista, J.; Beers, T.C.; Beifiori, A.; Berlind, A.A.; Bhardwaj, V.; Bizyaev, D.; Blake, C.H.; Blanton, M.R.; Blomqvist, M.; Bochanski, J.J.; Bolton, A.S.; Borde, A.; Bovy, J.; Brandt, W.N.; Brinkmann, J.; Brown, P.J.; Brownstein, J.R.; Bundy, K.; Busca, N.G.; Carithers, W.; Carnero, A.R.; Carr, M.A.; Casetti-Dinescu, D.I.; Chen, Y.; Chiappini, C.; Comparat, J.; Connolly, N.; Crepp, J.R.; Cristiani, S.; Croft, R.A.C.; Cuesta, A.J.; da Costa, L.N.; Davenport, J.R.A.; Dawson, K.S.; de Putter, R.; De Lee, N.; Delubac, T.; Dhital, S.; Ealet, A.; Ebelke, G.L.; Edmondson, E.M.; Eisenstein, D.J.; Escoffier, S.; Esposito, M.; Evans, M.L.; Fan, X.; Femenía Castellá, B.; Fernández Alvar, E.; Ferreira, L.D.; Filiz Ak, N.; Finley, H.; Fleming, S.W.; Font-Ribera, A.; Frinchaboy, P.M.; García-Hernández, D.A.; García Pérez, A.E.; Ge, J.; Génova-Santos, R.; Gillespie, B.A.; Girardi, L.; González Hernández, J.I.; Grebel, E.K.; Gunn, J.E.; Guo, H.; Haggard, D.; Hamilton, J.C.; Harris, D.W.; Hawley, S.L.; Hearty, F.R.; Ho, S.; Hogg, D.W.; Holtzman, J.A.; Honscheid, K.; Huehnerhoff, J.; Ivans, I.I.; Ivezić, Ž.; Jacobson, H.R.; Jiang, L.; Johansson, J.; Johnson, J.A.; Kauffmann, G.; Kirkby, D.; Kirkpatrick, J.A.; Klaene, M.A.; Knapp, G.R.; Kneib, J.P.; Le Goff, J.M.; Leauthaud, A.; Lee, K.G.; Lee, Y.S.; Long, D.C.; Loomis, C.P.; Lucatello, S.; Lundgren, B.; Lupton, R.H.; Ma, B.; Ma, Z.; MacDonald, N.; Mack, C.E.; Mahadevan, S.; Maia, M.A.G.; Majewski, S.R.; Makler, M.; Malanushenko, E.; Malanushenko, V.; Manchado, A.; Mandelbaum, R.; Manera, M.; Maraston, C.; Margala, D.; Martell, S.L.; McBride, C.K.; McGreer, I.D.; McMahan, R.G.; Ménard, B.; Meszaros, S.; Miralda-Escudé, J.; Montero-Dorta, A.D.; Montesano, F.; Morrison, H.L.; Muna, D.; Munn, J.A.; Murayama, H.; Myers, A.D.; Neto, A.F.; Nguyen, D.C.; Nichol, R.C.; Nidever, D.L.; Noterdaeme, P.; Nuza, S.E.; Ogando, R.L.C.; Olmstead, M.D.; Oravetz, D.J.; Owen, R.; Padmanabhan, N.; Palanque-Delabrouille, N.; Pan, K.; Parejko, J.K.; Parihar, P.; Pâris, I.; Pattarakijwanich, P.; Pepper, J.; Percival, W.J.; Pérez-Fournon, I.; Pérez-Ràfols, I.; Petitjean, P.; Pforr, J.; Pieri, M.M.; Pinsonneault, M.H.; Porto de Mello, G.F.; Prada, F.; Price-Whelan, A.M.; Raddick, M.J.; Rebolo, R.; Rich, J.; Richards, G.T.; Robin, A.C.; Rocha-Pinto, H.J.; Rockosi, C.M.; Roe, N.A.; Ross, A.J.; Ross, N.P.; Rossi, G.; Rubiño-Martín, J.A.; Samushia, L.; Sanchez Almeida, J.; Sánchez, A.G.; Santiago, B.; Sayres, C.; Schlegel, D.J.; Schlesinger, K.J.; Schmidt, S.J.; Schneider, D.P.; Schultheis, M.; Schwobe, A.D.; Scóccola, C.G.; Seljak, U.; Sheldon, E.; Shen, Y.; Shu, Y.; Simmerer, J.; Simmons, A.E.; Skibba, R.A.; Skrutskie, M.F.; Slosar, A.; Sobreira, F.; Sobock, J.S.; Stassun, K.G.; Steele, O.; Steinmetz, M.; Strauss, M.A.; Streblyanska, A.; Suzuki, N.; Swanson, M.E.C.; Tal, T.; Thakar, A.R.; Thomas, D.; Thompson, B.A.; Tinker, J.L.; Tojeiro, R.; Tremonti, C.A.; Vargas Magaña, M.; Verde, L.; Viel, M.; Vikas, S.K.; Vogt, N.P.; Wake, D.A.; Wang, J.; Weaver, B.A.; Weinberg, D.H.; Weiner, B.J.; West, A.A.; White, M.; Wilson, J.C.; Wisniewski, J.P.; Wood-Vasey, W.M.; Yanny, B.; Yèche, C.; York, D.G.; Zamora, O.; Zasowski, G.; Zehavi, I.; Zhao, G.B.; Zheng, Z.; Zhu, G.; Zinn, J.C. The Ninth Data Release of the Sloan Digital Sky Survey: First Spectroscopic Data from the SDSS-III Baryon Oscillation Spectroscopic Survey. *ApJS* **2012**, *203*, 21, [[arXiv:astro-ph.IM/1207.7137](https://arxiv.org/abs/1207.7137)]. doi:10.1088/0067-0049/203/2/21.
73. Véron-Cetty, M.P.; Véron, P. A catalogue of quasars and active nuclei: 13th edition. *A&A* **2010**, *518*, A10. doi:10.1051/0004-6361/201014188.
74. Pâris, I.; Petitjean, P.; Aubourg, É.; Myers, A.D.; Streblyanska, A.; Lyke, B.W.; Anderson, S.F.; Armengaud, É.; Bautista, J.; Blanton, M.R.; Blomqvist, M.; Brinkmann, J.; Brownstein, J.R.; Brandt, W.N.; Burtin, É.; Dawson, K.; de la Torre, S.; Georgakakis, A.; Gil-Marín, H.; Green, P.J.; Hall, P.B.; Kneib, J.P.; LaMassa, S.M.; Le Goff, J.M.; MacLeod, C.; Mariappan, V.; McGreer, I.D.; Merloni, A.; Noterdaeme, P.; Palanque-Delabrouille, N.; Percival, W.J.; Ross, A.J.; Rossi, G.; Schneider, D.P.; Seo, H.J.; Tojeiro, R.; Weaver, B.A.; Weijmans, A.M.; Yèche, C.; Zarrouk, P.; Zhao, G.B. The Sloan Digital Sky Survey Quasar Catalog: Fourteenth data release. *A&A* **2018**, *613*, A51, [[arXiv:astro-ph.GA/1712.05029](https://arxiv.org/abs/1712.05029)]. doi:10.1051/0004-6361/201732445.
75. Sbarufatti, B.; Treves, A.; Falomo, R.; Heidt, J.; Kotilainen, J.; Scarpa, R. ESO Very Large Telescope Optical Spectroscopy of BL Lacertae Objects. I. New Redshifts. *AJ* **2005**, *129*, 559–566, [[arXiv:astro-ph/0410692](https://arxiv.org/abs/astro-ph/0410692)]. doi:10.1086/427138.
76. Barkhouse, W.A.; Hall, P.B. Quasars in the 2MASS Second Incremental Data Release. *AJ* **2001**, *121*, 2843–2850, [[arXiv:astro-ph/0101270](https://arxiv.org/abs/astro-ph/0101270)]. doi:10.1086/320377.
77. Beckmann, V.; Gehrels, N.; Shrader, C.R.; Soldi, S. The First INTEGRAL AGN Catalog. *ApJ* **2006**, *638*, 642–652, [[arXiv:astro-ph/0510530](https://arxiv.org/abs/astro-ph/0510530)]. doi:10.1086/499034.
78. Snellen, I.A.G.; McMahan, R.G.; Hook, I.M.; Browne, I.W.A. Automated optical identification of a large complete northern hemisphere sample of flat-spectrum radio sources with  $[formmu1]S_{6cm} > 200$  mJy. *MNRAS* **2002**, *329*, 700–746, [[arXiv:astro-ph/0110136](https://arxiv.org/abs/astro-ph/0110136)]. doi:10.1046/j.1365-8711.2002.05049.x.
79. Ebdon, L.; Evans, E.H.; Fisher, A.; Hill, S.J. *An Introduction to Analytical Atomic Spectrometry*; J. Wiley & Sons, 1998.
80. Noll, S.; Kausch, W.; Barden, M.; Jones, A.M.; Szyszka, C.; Kimeswenger, S.; Vinther, J. An atmospheric radiation model for Cerro Paranal. I. The optical spectral range. *A&A* **2012**, *543*, A92, [[arXiv:astro-ph/1205.2003](https://arxiv.org/abs/astro-ph/1205.2003)]. doi:10.1051/0004-6361/201219040.
81. Clough, S.A.; Shephard, M.W.; Mlawer, E.J.; Delamere, J.S.; Iacono, M.J.; Cady-Pereira, K.; Boukabara, S.; Brown, P.D. Atmospheric radiative transfer modeling: a summary of the AER codes. *J. Quant. Spec. Radiat. Transf.* **2005**, *91*, 233–244. doi:10.1016/j.jqsrt.2004.05.058.
82. Rothman, L.S.; Gordon, I.E.; Barbe, A.; Benner, D.C.; Bernath, P.F.; Birk, M.; Boudon, V.; Brown, L.R.; Campargue, A.; Champion, J.P.; Chance, K.; Coudert, L.H.; Dana, V.; Devi, V.M.; Fally, S.; Flaud, J.M.; Gamache, R.R.; Goldman, A.; Jacquemart, D.; Kleiner, I.; Lacome, N.; Lafferty, W.J.; Mandin, J.Y.; Massie, S.T.; Mikhailenko, S.N.; Miller, C.E.; Moazzen-Ahmadi, N.; Naumenko, O.V.; Nikitin,

- 
- A.V.; Orphal, J.; Perevalov, V.I.; Perrin, A.; Predoi-Cross, A.; Rinsland, C.P.; Rotger, M.; Šimečková, M.; Smith, M.A.H.; Sung, K.; Tashkun, S.A.; Tennyson, J.; Toth, R.A.; Vandaele, A.C.; Vander Auwera, J. The HITRAN 2008 molecular spectroscopic database. *J. Quant. Spec. Radiat. Transf.* **2009**, *110*, 533–572. doi:10.1016/j.jqsrt.2009.02.013.
83. Bagnulo, S.; Cox, N.L.J.; Cikota, A.; Siebenmorgen, R.; Voshchinnikov, N.V.; Patat, F.; Smith, K.T.; Smoker, J.V.; Taubenberger, S.; Kaper, L.; Cami, J.; LIPS Collaboration. Large Interstellar Polarisation Survey (LIPS). I. FORS2 spectropolarimetry in the Southern Hemisphere. *A&A* **2017**, *608*, A146, [[arXiv:astro-ph.SR/1710.02439](https://arxiv.org/abs/1710.02439)]. doi:10.1051/0004-6361/201731459.
84. Siebenmorgen, R.; Voshchinnikov, N.V.; Bagnulo, S.; Cox, N.L.J.; Cami, J.; Peest, C. Large Interstellar Polarisation Survey. II. UV/optical study of cloud-to-cloud variations of dust in the diffuse ISM. *A&A* **2018**, *611*, A5, [[arXiv:astro-ph.GA/1711.08672](https://arxiv.org/abs/1711.08672)]. doi:10.1051/0004-6361/201731814.